Journal of Sedimentary Research, 2026, v. 96, 723–750
Research Article
DOI: 10.2110/jsr.2025.098

EXPOSURE AND KARST DEVELOPMENT ON AN AGGRADATIONAL SHELF MARGIN, EDIACARAN BIRBA PLATFORM, SOUTH OMAN SALT BASIN

THEODORE M. PRESENT,[1] ERWIN W. ADAMS,[2] KRISTIN D. BERGMANN,[3] ABDULRAHMAN AL HARTHY,[4] ZUWAINA AL RAWAHI,[4] AND JOHN P. GROTZINGER[1]

[1]*Division of Geological and Planetary Science, California Institute of Technology, Pasadena, California 91125, U.S.A.*
[2]*Shell Global Solutions International B.V., Carel van Bylandtlaan 16, 2596 HR Den Haag, The Netherlands*
[3]*Department of Earth, Atmospheric and Planetary Sciences, Massachusetts Institute of Technology, Cambridge, Massachusetts 02139, U.S.A.*
[4]*Petroleum Development Oman, Muscat, 100, Sultanate of Oman*
e-mail: tpresent@caltech.edu

ABSTRACT: **Intraformational dolomite breccias observed in three cores retrieved from the subsurface Birba Formation in Oman are interpreted as exposure and karst features in the amalgamated Basal Ara Carbonate (BAC) units of the Ediacaran–Cambrian Ara Group of the South Oman Salt Basin (SOSB). Karst breccias developed during BAC exposure are differentiated from depositional breccias in supratidal and subtidal facies by core and petrographic observations. Well-developed karst-collapse breccias are limited in scale, and much of the brecciation is in-situ compaction of solution-enlarged fractures, forming mosaic breccias in already permeable intertidal-to-supratidal facies that constituted a shelf-crest shoal complex with positive relief. Petrographic fabrics and chemical imaging of breccias indicate that karsting was followed by reinundation of the BAC by suboxic marine or mixed marine–meteoric fluids, consistent with limited exposure durations at high-frequency or composite sequence-scale disconformities. The observations complement previous work on more protected evaporite–carbonate stringers that lack clear evidence of well-developed exposure surfaces. Integrated stratigraphic and petrographic analysis is necessary to identify sequence boundaries amid accumulated exposure inherent in supratidal facies. The supratidal barrier complex in the BAC developed in a stable and aggradational accommodation regime at a key tectonic transition in the SOSB, when, just before the advancement of a foreland thrust belt associated with the latest assembly of Gondwana, basin accommodation began increasing markedly. These conditions generated a well-developed hydrographic barrier, resulting in the predominant architecture of the Ara Group, in which lowstand evaporitic facies conformably overlie carbonate platforms.**

INTRODUCTION

Karst formations and paleokarst features in Phanerozoic strata, especially those associated with major sequence and supersequence boundaries, are generally well documented and understood (Esteban and Klappa 1983; James and Choquette 1988). Seismic-scale stratigraphic features include angular unconformities, disconformities, channel incisions, interrupted or irregular to jagged strata, and reticulated to polygon-like landscapes (Vahrenkamp et al. 2004; Grélaud et al. 2006; Purkis et al. 2010; Cross et al. 2021). Characteristic petrographic facies and fabrics include particular vug and cavern network patterns, heterolithic breccias sourced from lithologically diverse overburden, speleothems and flowstones, and pedogenic fabrics often related to plant growth (Gonzalez and Lohmann 1988; Kerans 1993; Wright 1994; Lucia 1995; Rankey and Bachtel 1998; Loucks 1999; Nolting et al. 2024). In the subsurface, where many diagnostic geometries cannot be observed, differentiating paleokarsts from other breccias and permeable carbonate strata based on seismic geometries, wireline log features, and fabric and petrographic observations apparent in core is challenging.

In Precambrian strata, paleokarsts are documented mainly from outcrop exposures and major unconformities. Several paleokarsts have been recognized at the top of Neoproterozoic strata, below an unconformity constituting the Precambrian–Cambrian boundary, with karstification during latest Neoproterozoic or earliest Cambrian time (Teitz 1985; Teitz and Mountjoy 1989; Urlwin 1997; Mathieu et al. 2017; Ding et al. 2019; He et al. 2019; Tang et al. 2021; Gómez-Pérez et al. 2024a; Bergmann et al. 2025). There are few other wholly Neoproterozoic-age karsts, with intra-Ediacaran-age (Cozzi et al. 2004; Praekelt et al. 2008; Bergmann 2013; Ding et al. 2019; De Wit et al. 2020; Gómez-Pérez et al. 2024a; Bergmann et al. 2025), Cryogenian-age (Kenny and Knauth 1992; James et al. 2001; Halverson et al. 2005; Petterson et al. 2011; Santos et al. 2022, 2023), and Tonian-age karsted surfaces (Mustard and Donaldson 1990; Turner and Long 2012). Some Mesoproterozoic paleokarsts are recognized by large-scale brecciation, cave collapse, and compaction features (Kerans and Donaldson 1988; Pelechaty et al. 1991). However, identification of other older paleokarsts is hampered by much younger burial diagenesis or recent surficial weathering, and is sometimes controversial or ambiguous (Jolliffe 1955; Shride 1967; Beeunas and Knauth 1985; Machado 1987; Vahrenkamp and Rossinsky 1987; Kenny and Knauth 1992; Skotnicki and Knauth 2007; Fralick and Riding 2015).

Unusual Precambrian peritidal facies further complicate understanding and recognition of exposure. Precambrian carbonate platforms sometimes contain supratidal facies associations that are rare in modern carbonate

Published Online: August 2026
 1527-1404/26/096-723

sedimentary environments: tepee-pisolite complexes comprising meter-scale arrays of buckled carbonate sheets and coated-grain accumulations, with sufficient paleogeomorphic relief to have formed hydrographic barriers (Assereto and Kendall 1977; Grotzinger and James 2000). Identification and characterization of these carbonate barrier complexes is critical for understanding platform-scale hydrology, exposure frequency, and the development of karst features (Kendall 1969). Distinguishing significant tectonically or eustatically derived sequence boundaries from minor accumulations of exposure inherent to supratidal facies remains a persistent challenge.

In addition to serving as major hydrocarbon resources, the terminal Neoproterozoic chemical sediments (carbonates, evaporites, and silicilytes) of the Ara Group, Oman record the tectonic evolution of the later stages of Gondwana assembly, the extinction of early calcareous fossils near the Precambrian–Cambrian boundary, and large marine carbon- and sulfur-isotope excursions (Matter and Burns 1993; Amthor et al. 2003; Al-Siyabi 2005; Allen 2007; Bowring et al. 2007; Fike and Grotzinger 2008; Gómez-Pérez et al. 2024b; Bergmann et al. 2025). The Ara Group unconformably overlies the Nafun Group, and the unconformity is karsted in outcrops in the Huqf region in eastern Oman and Jabal Akhdar in northern Oman (Gorin et al. 1982; Cozzi et al. 2004; Nicholas and Gold 2012; Bergmann 2013; Gómez-Pérez et al. 2024a; Bergmann et al. 2025). However, well-developed exposure surfaces and karst have not been recognized in the methodically studied vast number of cores recovered from the subsurface Ara Group in the South Oman Salt Basin (SOSB) (Fig. 1A). Despite the presence of shallowing peritidal and supratidal carbonates, an abrupt transition into evaporite deposition is systematically recorded, feeding the conundrum that lowstand evaporites rest directly on top of highstand carbonate-platform systems requiring durable tectonic subsidence (Schröder et al. 2003; Grotzinger and Al-Rawahi 2014).

Brecciated intervals in Birba Formation (basal part of the Ara Group, Fig. 1B) carbonate strata were tentatively ascribed to paleokarst and exposure processes by previous Petroleum Development Oman studies (unpublished). We undertook a lithofacies, paragenetic, and geochemical study of these strata to better evaluate the origin of the breccias, developing criteria to distinguish karst breccias from depositional or other diagenetic breccias in cores of peritidal carbonate facies. In this process, we establish a depositional model for the BAC shelf margin, whilst seismic data provide the spatial and stratigraphic context. We identify sequence boundaries from facies stacking patterns, an approach necessitated by the pervasive brecciation inherent in supratidal facies and by the absence of thick evaporites that mark cycle boundaries elsewhere in the Ara Group. Identification of exposure surfaces in basal Ara Group carbonates might provide stratigraphic markers that improve correlations in the amalgamated Birba carbonates, through the segmented SOSB, potentially across Oman, and in related eastern Gondwana tectonic basins.

GEOLOGIC SETTING

Oman occupied a position between the converging Arabian–Nubian Shield and the Greater Indian Shield during Neoproterozoic–earliest Cambrian closure of the Mozambique Ocean and final assembly of Gondwana (Johnson and Woldehaimanot 2003; Allen 2007; Gómez-Pérez et al. 2024b; Gómez-Pérez and Morton 2025). Several tectonic basins that developed during this convergence were filled by volcanic and sedimentary strata of the Huqf Supergroup (Gorin et al. 1982; Clarke 1988). During latest deposition of the Huqf Supergroup, depositional patterns shifted markedly. The Nafun Group comprises regionally expansive mixed siliciclastic and carbonate stratigraphy that filled a broad, slowly subsiding basin, with shallower depositional areas in the east and northeast. The overlying Ara Group was deposited in N–S-trending, fault-bounded troughs and structural highs with differential subsidence, and comprises carbonate, evaporite, organic-rich shale, and chert strata accompanied by volcanic ash beds (Fig. 1B) (Mattes and Conway Morris 1990; Amthor et al. 2005; Allen 2007; Bowring et al. 2007; Grotzinger and Al-Rawahi 2014; Gómez-Pérez et al. 2024a; Gómez-Pérez and Morton 2025). One of these basins, the SOSB, is bounded by a western thrust and transpressional front (Western Deformation Front) and an eastern structural arch (Eastern Flank) (Fig. 1A) (Loosveld et al. 1996). During earliest Cambrian time, uplifted terranes along the Western Deformation Front provided siliciclastic material deposited in a clastic wedge that interfingered with and eventually blanketed upper Ara chemical sediments (Al-Marjeby and Nash 1986; Mattes and Conway Morris 1990; Loosveld et al. 1996; Amthor et al. 2005; Allen 2007; Bowring et al. 2007; Grotzinger and Al-Rawahi 2014; Gómez-Pérez et al. 2024a, 2024b; Gómez-Pérez and Morton 2025).

The Ara Group unconformably overlies the Nafun Group as recognized by subsurface seismic data and borehole dipmeter logs (Forbes et al. 2010; Grotzinger and Al-Rawahi 2014; Gómez-Pérez et al. 2024a) and as observed in outcrop as the base-Ara unconformity (Mattes and Conway Morris 1990; Cozzi et al. 2004; Nicholas and Gold 2012; Bergmann 2013; Gómez-Pérez et al. 2024a). The Nafun–Ara unconformity retained significant topographic relief, partially because of the reactivation of older Cryogenian-age rift structures during the development of the unconformity. This is represented by regional thinning of Nafun Group strata towards the northwest, followed by a shift to north–south-striking depositional patterns controlled by ca. 40-km-wide horsts and grabens during earliest Ara Group deposition (Amthor et al. 2005; Allen 2007; Gómez-Pérez et al. 2024a). The Nafun–Ara unconformity developed in the SOSB during an interval older than 546.7 ± 0.92 Ma (Bowring et al. 2007) (Fig. 1) and younger than 553.4 ± 4.1 Ma (Cantine et al. 2024).

The Ara Group predominantly comprises anhydrite and halite evaporites with interbedded dolomitic carbonate units, called "stringers" (Mattes and Conway Morris 1990; Schröder et al. 2003, 2005; Al-Siyabi 2005; Amthor et al. 2005; Grotzinger and Al-Rawahi 2014; Gómez-Pérez et al. 2024a). In the Southern Carbonate Domain of the SOSB, at least six evaporite–carbonate cycles are recognized in the Ara Group (Fig. 1) (Forbes et al. 2010; Grotzinger and Al-Rawahi 2014). The three lowermost cycles define the Birba Formation, which is best developed in the eastern part of the Southern Carbonate Domain. Here, massive carbonates, often referred to as the Basal Ara Carbonate (BAC), are amalgamated across multiple carbonate cycles and lack the interbedded evaporites that mark cycle boundaries elsewhere in the Ara Group (Mattes and Conway Morris 1990). The Birba Formation is defined in reference well Shamah-1, where the base is defined by a dipmeter break associated with the angular unconformity with the underlying Buah Formation of the Nafun Group. The absence of evaporite markers complicates stratigraphic correlation between the Birba Platform and coeval stringers, but seismic-based regional correlations are supported by the presence of interbedded volcanic ashes (Amthor et al. 2003; Bowring et al. 2007; Forbes et al. 2010). The basin between the eastern platform margin of the BAC and the eastern flank of the SOSB, called the Athel Trough, contains thinner basinal carbonates shed from the platform margin, as well as deepwater shales, carbonate, and laminated cherts (silicilyte) (Amthor et al. 2005, 2015; Schröder and Grotzinger 2007; Rajaibi et al. 2015).

Regional seismic and well data show that basal siliciclastic—at least in part volcaniclastic—sediments laterally interfinger with the BAC and onlap older Buah Platform carbonates, which developed atop remnant and reactivated structural highs (Fig. 2A–F) (Bowring et al. 2007; Forbes et al. 2010; Cantine et al. 2024; Gómez-Pérez et al. 2024a). In well X-2, argillaceous dolomites and shales mark the base of the BAC (Clarke 1988; Forbes et al. 2010). Deposition of the lowest sequence of carbonate strata in the BAC, referred to as the A0C, largely flattened pre-Ara structural and topographic relief. Seismic geometries further show that the Birba Platform became increasingly aggradational during A1C time, creating a steep north–south-trending escarpment-type platform margin in the east. This north–south structural grain with alternating highs and lows controlled facies distribution and promoted basinal restriction on a broad intra-platform shelf west of the margin (Fig. 1A). Compared to the steep

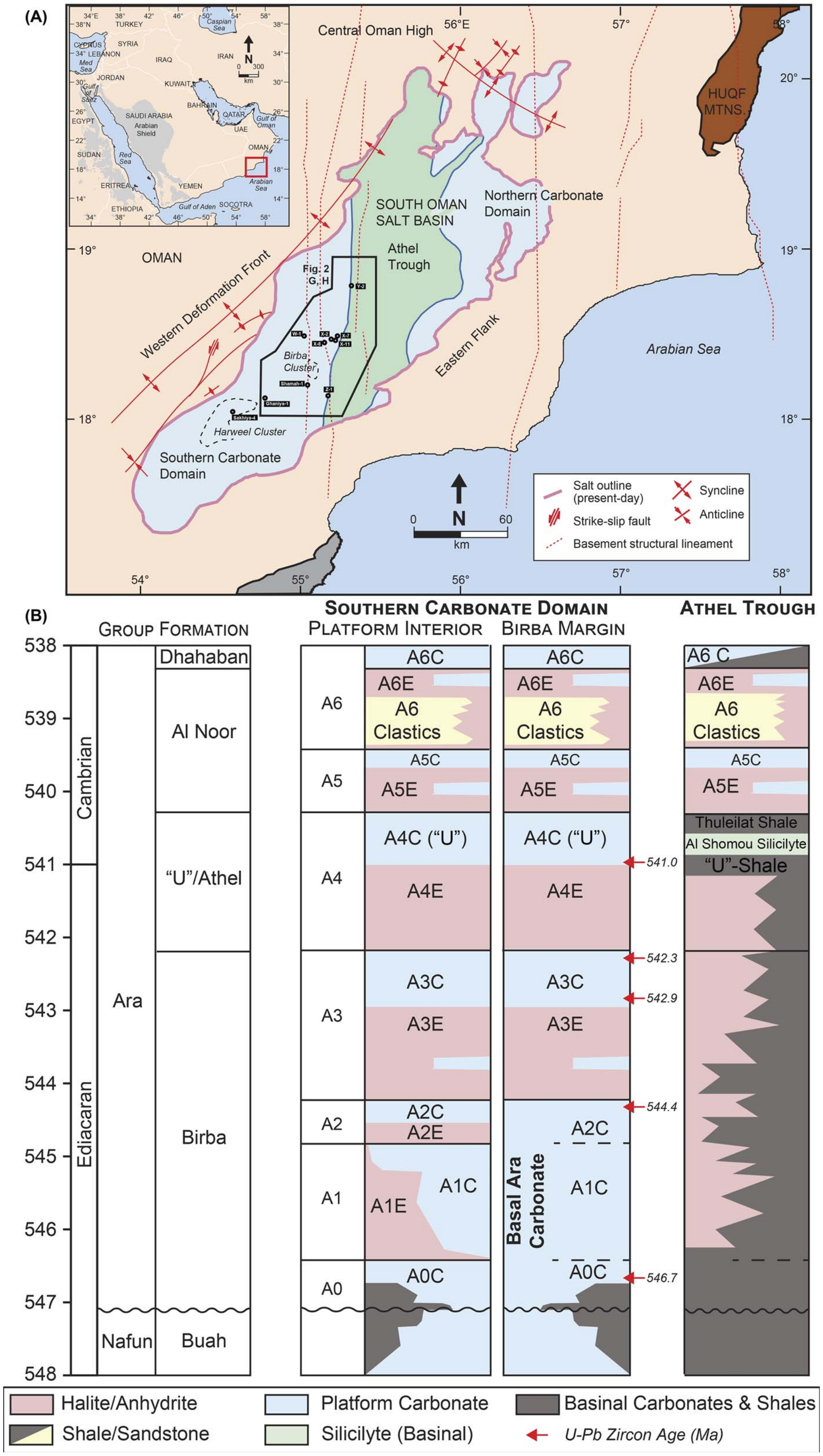

FIG. 1.—Neoproterozoic and Cambrian lithostratigraphy of southern Oman. **A)** Regional tectonostratigraphic map of the SOSB and surrounding area of southern Oman (inset), modified from Amthor et al. (2005) and Al-Siyabi (2005), with north–south-trending basement lineaments from Stuart-Smith et al. (2007). The black polygon denotes the eastern margin of the Southern Carbonate Domain shown in Figure 2. **B)** Lithostratigraphy modified from Amthor et al. (2005) and Grotzinger and Al-Rawahi (2014). U–Pb ages are from Bowring et al. (2007) and Forbes et al. (2010).

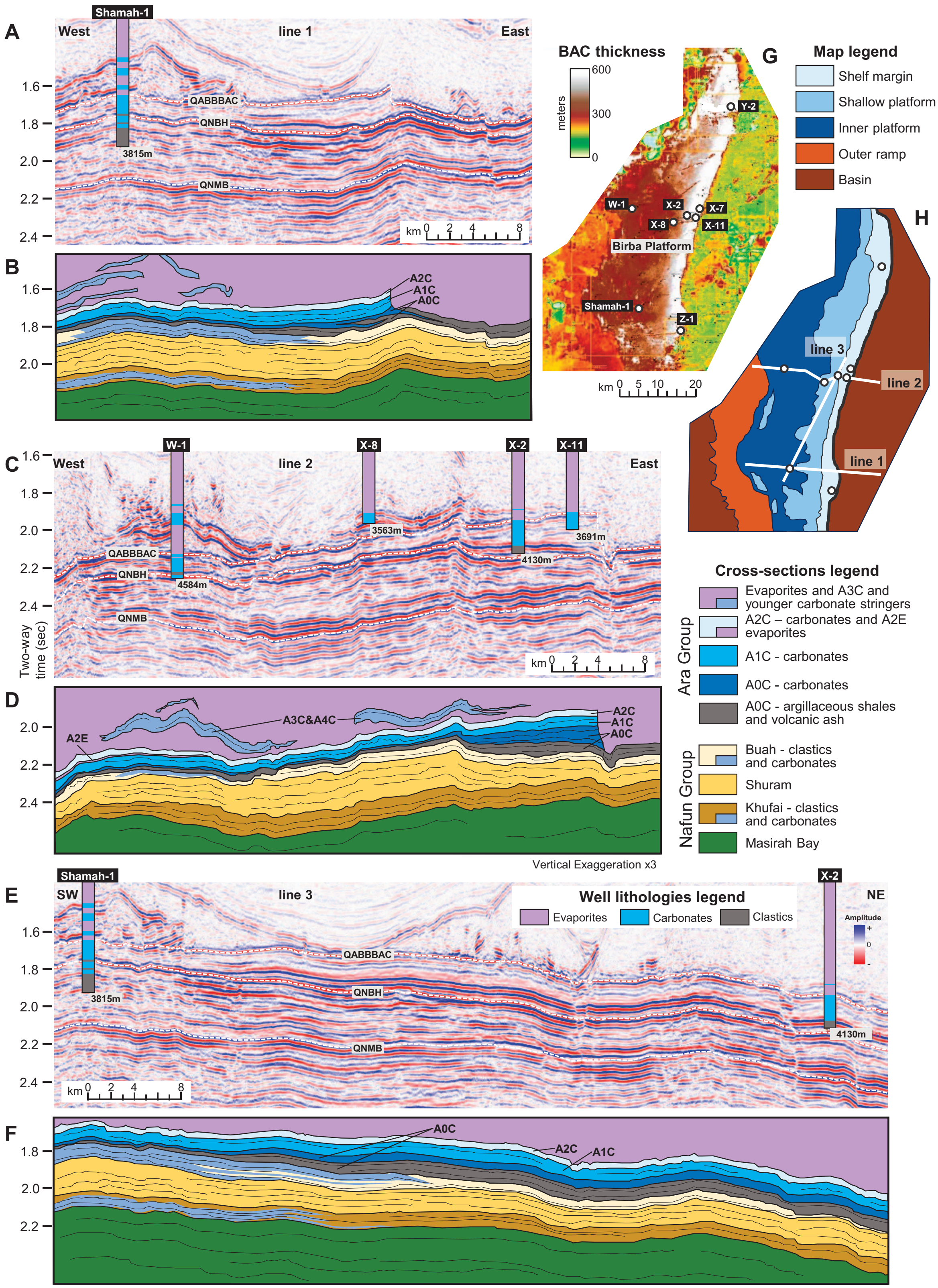

FIG. 2.—Seismic stratigraphic context of the Birba Platform. **A)** East–west seismic line through the reference well for the Birba Formation Shamah-1. The dotted white lines are the interpreted top of the Masirah Bay (QNMB) and Buah (QNBH) formations, and BAC platform (QABBBAC) according to Forbes et al. (2010). **B)** Interpreted seismic line 1 showing the formation and cycle subdivisions for the Nafun and Ara groups. The more chaotic seismic facies (see Part A) correlates to Buah Formation carbonates, penetrated by well Shamah-1, with a ramp-like geometry; to the east the chaotic seismic facies passes into continuous seismic reflectors interpreted as basinal sediments. The presence of Khufai Formation carbonates is an interpretation. **C)** East–west seismic line 2 through wells W-1, X-2, X-8, and X-11. **D)** Interpretation of

eastern platform margin, the western edge of the Birba Platform is recognized by a more gradual, ramp-type margin. In well W-1, anhydrite and halite are interbedded with the BAC and correlate to the A2E (Fig. 2D). Farther west, a platform-interior basin separates the Birba Cluster from archetypal carbonate stringers developed above another preexisting structural high, called the Harweel Cluster, all of which are separated by evaporite strata (Fig. 2C, D, H) (Mattes and Conway Morris 1990; Amthor et al. 2005). This structural low between the Birba and Harweel clusters contains broad evaporitic basinal facies well represented by deepwater ramp and slope mudstones in well Ghaniya-1 (Fig. 1A) (Al-Siyabi 2005; Grotzinger and Al-Rawahi 2014).

SAMPLES AND METHODS

We examined the lithologies, diagenesis, and geochemistry of three wells situated along strike of the BAC escarpment-type shelf margin, where the thickest BAC isopachs were determined from subsurface seismic data (Fig. 2G). From south to north, wells Z-1, X-7, and Y-2 were examined. The BAC is 448 m thick in Z-1 and 502 m thick in X-7; Y-2 was drilled to 477 m beneath the salt but did not reach the base of the BAC. The southernmost and shallowest well, Z-1, was spudded in 1977, and six cores were obtained between 2394.5 m and 2774.6 m depth. Three nearly continuous cores from X-7, spudded in 2008, were obtained between 3575.0 m and 3635.8 m depth. Three cores of the northernmost and deepest well, Y-2, spudded in 2015, were obtained between 5299.0 m and 5484.8 m depth. Detailed core descriptions are reported in the Supplementary Material.

Cored strata in the three wells comprises 88 m total thickness, and 63 core samples were selected for further study. From these, 25 thin sections were prepared with blue-stained epoxy to highlight pores and stained with Alizarin Red S to differentiate calcite from dolomite (Friedman 1959). Ten of these were prepared with isopropyl alcohol instead of water to preserve halite. Thin sections were examined with an optical petrographic microscope under polarized light.

From 22 sample slabs or thin sections, 46 microscale X-ray fluorescence (μXRF) chemical images were acquired using a Bruker M4 Tornado. Chemical images were obtained by illuminating the sample under 2 mbar vacuum with a polycapillary optic-focused rhodium X-ray source, which was excited to 50 kV with a 600 μA current. The energy spectrum of fluorescent X-rays was detected by two 30 mm^2 silicon drift detectors. Most chemical images were obtained with primary beam radiation filtered with a 100 μm Al foil to improve transition-metal-detection limits, permitting construction of composite chemical images with information content similar to cathodoluminescence petrography but with Fe and Mn energy discrimination. A nominal pixel size of 20 μm and an average pixel dwell time of 30 ms were found to efficiently capture much of the chemical contrast in samples. For some regions of interest, additional maps were obtained without primary-beam radiation filters and with longer dwell times (up to 200 ms). Energy-spectral overlaps, pile-up-detector artifacts, and escape-detector artifacts were deconvolved using Bruker M4 software v. 1.5, and standardless fundamental-parameter software methods were used to produce semiquantitative estimates of metal concentrations in an assumed carbonate matrix.

RESULTS

Lithofacies Descriptions

Cored intervals consist nearly entirely of dolomite with minor siliciclastic silty dolomite; calcite is rare to absent (present only as a minor pore-filling cement in Y-2), although several petrographic fabrics discussed below suggest that dolomite is a replacement mineral after primary calcite and aragonite. Ten lithofacies were identified by depositional texture, grain type, and sedimentary structures. Graphic logs of cored intervals of Y-2, X-7, and Z-1 are shown in Figure 3. These lithofacies are largely consistent with previous lithofacies classifications for Ara Group carbonate stringers by Schröder et al. (2003) and Grotzinger and Al-Rawahi (2014).

Pisoid Rudstone and Void-Filling Cement Boundstones

Gravel-size coated grains form thin to medium beds in Y-2 and X-7. Pisoid morphologies include concentrically laminated, well-rounded, millimeter to centimeter clasts that have spherical and composite shapes (Fig. 4A, B). Associated oncoids have irregularly laminated tabular (Fig. 4E), aggregate (Fig. 4F), and reniform shapes. Pisoids are moderately sorted and contain pockets of very coarse ooid sand, and often have a fitted fabric cemented by isopachous marine cements (Fig. 4A).

Subhorizontal and subvertical fractures and vuggy, solution-enlarged interparticle pores up to 40 cm thick are filled by isopachous, botryoidal, festoon, and pendant cements (Fig. 4C). Isopachous and botryoidal cements are also present as up to decimeter-thick coatings on oncoid rudstones, brecciated mudstones, and intraclast rudstones (Fig. 4D, F).

Fenestral-Laminated and Stromatolitic Boundstones

Very thick beds in X-7 and Y-2 consist of thinly to thickly laminated dolomite with cuspate, crinkly, tufted, and pustular laminae. Laminae are defined mainly by millimeter-scale oblong fenestral pores (Fig. 5A). Where pustules formed 2- to 6-cm-high stromatolites, laminae are chaotic, discontinuous, and frequently overhanging, and sometimes intercalated with intraclast grainstones and radial or festoon cements (Fig. 5B). In some cases, subvertical fractures with millimeter-scale apertures cut through laminae and are lined with similar crinkly-laminated dolomite (Fig. 5C). Fenestral pores, especially at the cores of pustules, are enlarged into centimeter-scale irregular vugs. In some core intervals, thick beds of fenestral-laminite boundstone are brecciated into centimeter-scale tabular intraclasts (Fig. 5D).

Nodular, Laminated, and Brecciated Mudstones–Packstones

Nodular mudstones to packstones are very thin- to thin-bedded and sometimes include evaporite molds (Fig. 6A) or anhydrite nodules with evidence of soft-sediment compaction (Fig. 6B) around them. Some mudstone beds are brecciated (Fig. 6C), forming centimeter-scale tabular intraclasts similar to those in fenestral-laminated boundstones. Brecciated mudstones–wackestones have isopachous bladed-dolomite cements lining interparticle pores and fractures (Fig. 6D).

←

seismic line 2, an escarpment-type margin on the eastern edge of the Birba Platform. Note the distal part of the Buah Formation carbonate ramp system penetrated in well W-1. **E)** SW–NE seismic line connecting through wells Shamah-1 and X-2. **F)** Interpretation of line 3 illustrating the depositional thinning to the NE of the Buah Formation carbonate ramp, whereas the Birba Formation thickens. Note onlap of A0C clastics onto tilted Buah Formation carbonates. The A0C cycle of the Birba Formation also thickens to the NW; the A1C and A2C are overall isopachous and aggradational. **G)** BAC isochore map measured between the QABBBAC and QNBH. H) Environment-of-deposition map for the BAC platform. The eastern edge is recognized by an escarpment margin (typified by rapid thickness change seen in Part G), whereas the western edge is more gradual and characterized by a ramp-type margin.

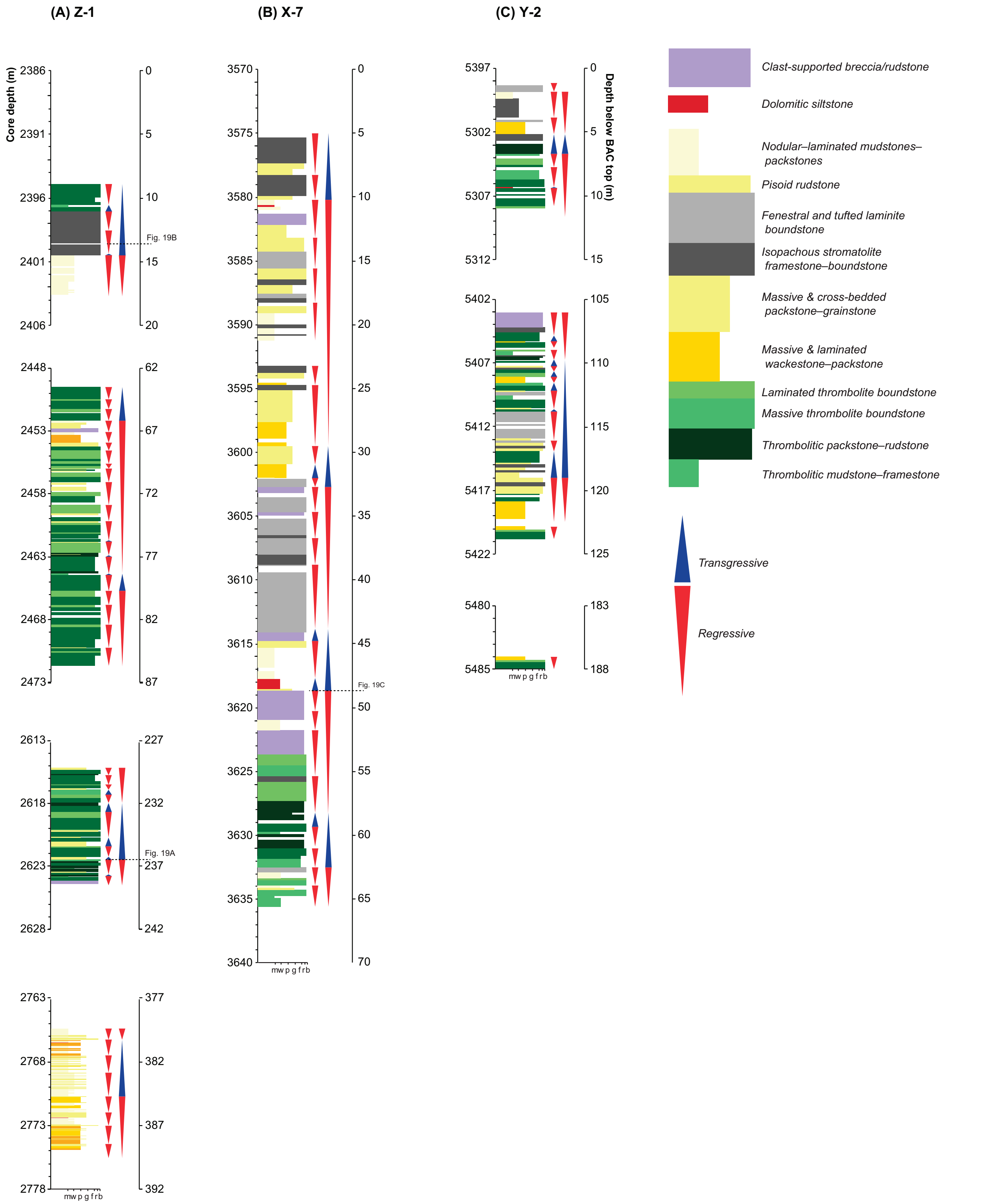

FIG. 3.—Graphic logs of BAC shelf-margin cores. Depths on the left side of logs are drill depth, and depths on the right side of logs are distance below the top of the BAC, chosen at the anhydrite–carbonate transition.

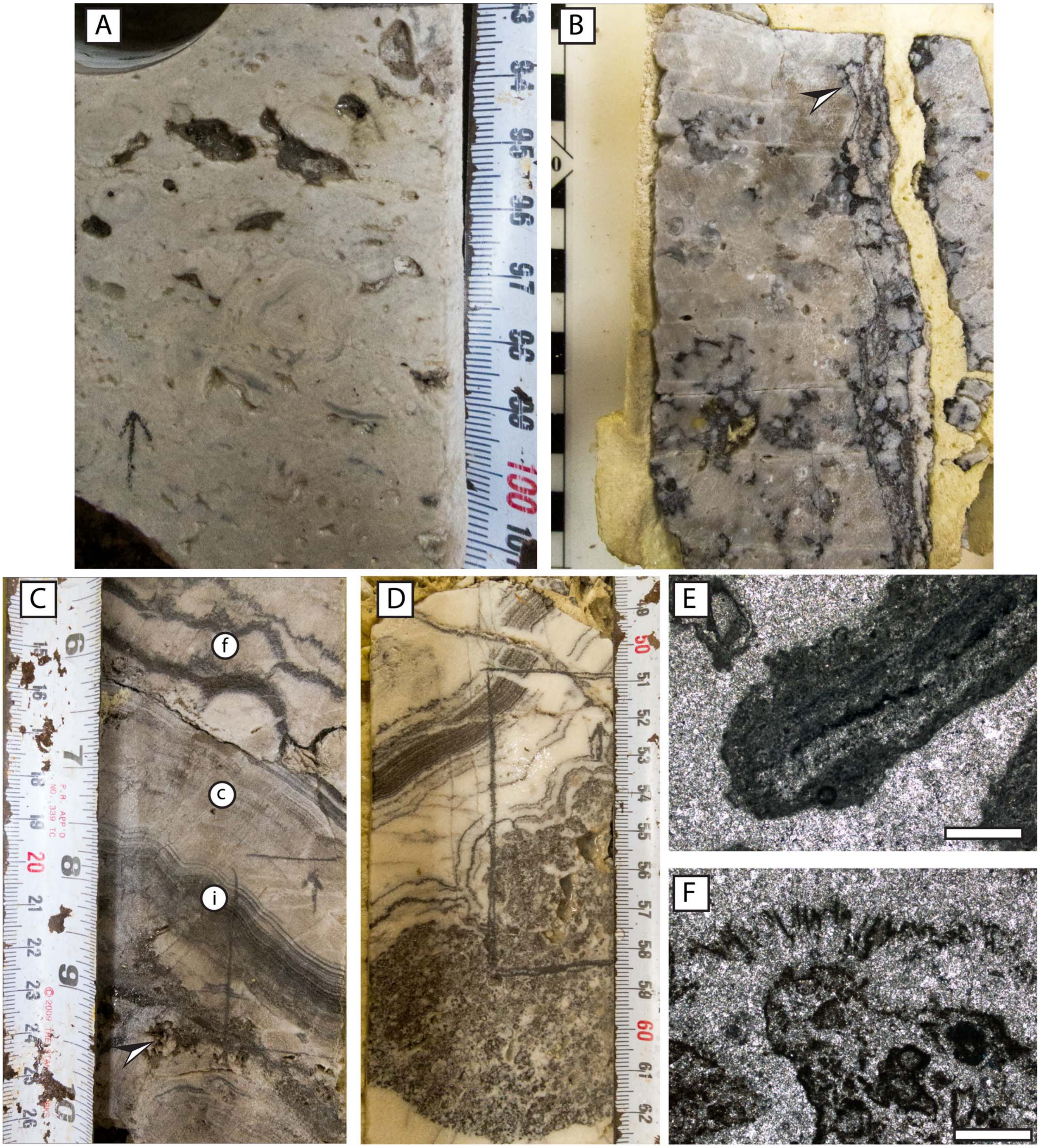

FIG. 4.—Pisoid rudstone and void-filling-cement boundstones interpreted as supratidal tepee-pisolite complexes. **A)** Reverse-graded pisoid rudstone with fitted fabric, X-7 3593.97 m. **B)** Pisoid rudstone with intraclasts in a solution-enlarged vertical fracture; arrow marks scalloped fracture margin, Y-2 5416.9 m. **C)** Isopachous (i), columnar (c), and festoon (f) cements interpreted as a sheet crack in fenestral and stromatolitic boundstone with evaporite molds (arrows), Y-2 5415.2 m. **D)** Intraclast rudstone coated by isopachous laminated cement, Y-2 5406.56 m. **E)** Tabular oncoid with intraclast nucleus, 500 µm scale bar, X-7 3593.59 m. **F)** Aggregate grain oncoid with dark micrite envelopes on grain and fringing cement, 500 µm scale bar, Y-2 5406.56 m. Orthorhombic fringe-cement terminations suggest that primary mineralogy was aragonite.

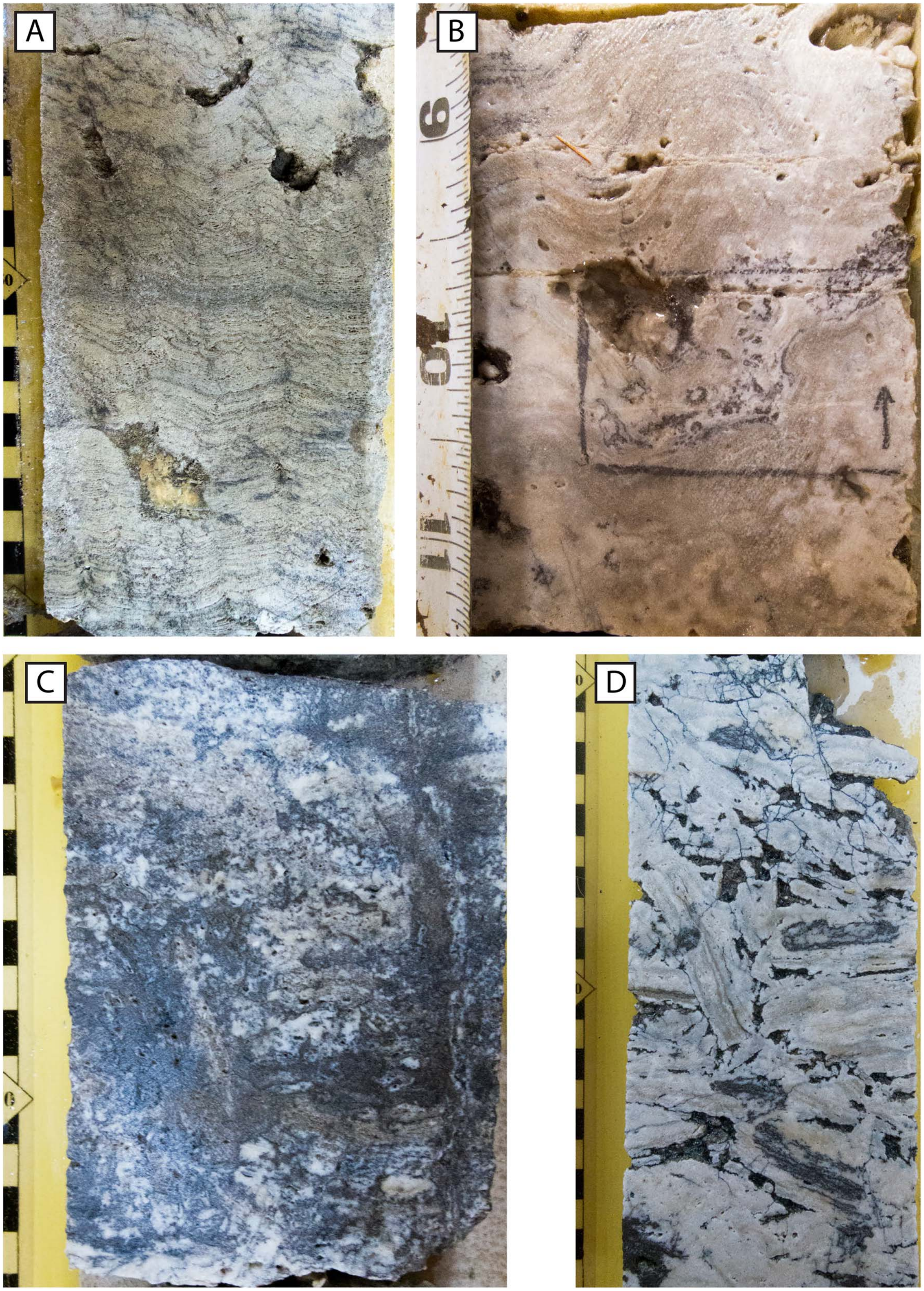

FIG. 5.—Fenestral-laminated-boundstone facies interpreted as intertidal microbial flats. **A)** Fenestral-laminated boundstone with cuspate laminae defined by millimeter-scale fenestral pores, X-7 3608.5 m. **B)** Tufted and pustular fenestral laminite, Y-2 5413.26 m. **C)** Vertical shrinkage crack lined by crinkly laminated dolomite in fenestral laminite, X-7 3613.7 m. **D)** Brecciated intraclast rudstone composed of tabular fenestral and crinkly laminated boundstone clasts, X-7 3602.9 m.

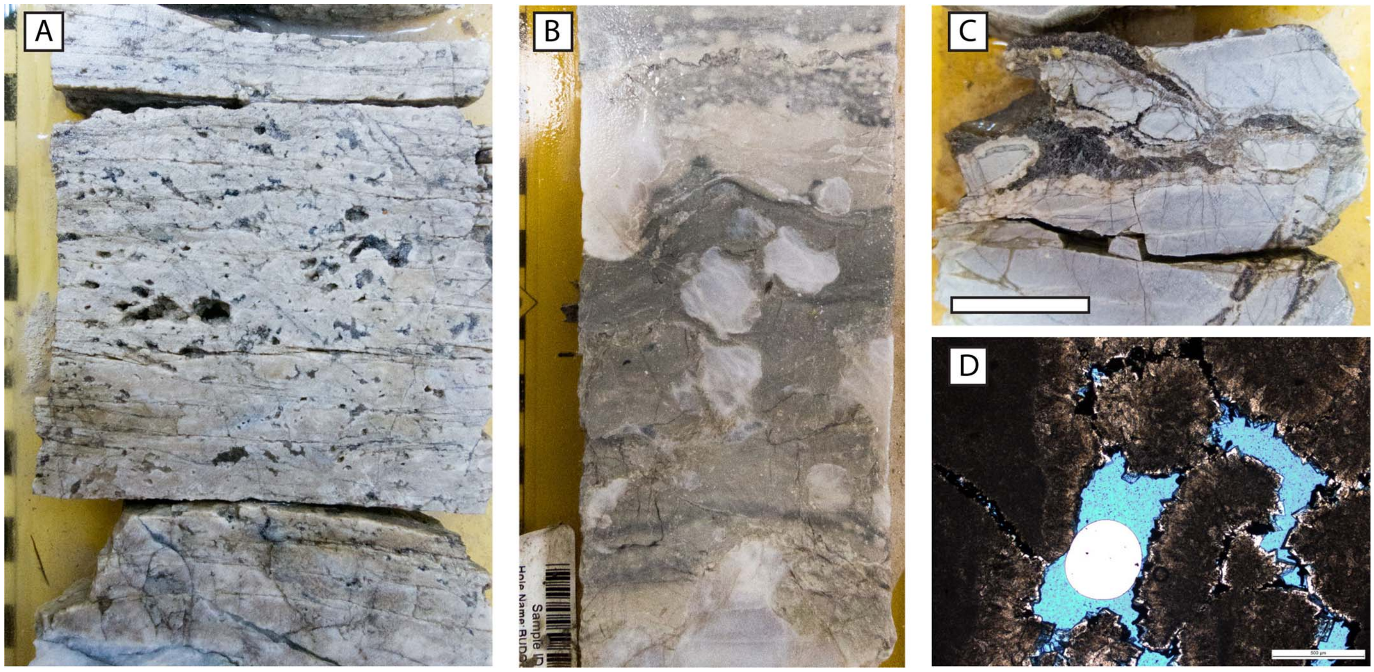

FIG. 6.—Nodular- and laminated-mudstone–packstone facies interpreted to have formed in an evaporitic, subtidal lagoon. **A)** Wavy laminated packstone with vuggy pores interpreted to have been evaporite molds, X-7 3618.8 m. **B)** Poorly laminated mudstone with anhydrite nodules, X-7 3580.9 m. **C)** Brecciated mudstone, 4 cm scale, X-7 3616.7 m. **D)** Mudstone–packstone brecciated into intraclast grainstone with isopachous bladed-dolomite cement lining grains, Z-1 2401.64 m.

Silty Peloid Mudstones–Packstones

A distinctive, stylolitic, thin bed of poorly sorted peloid packstone is observed in Z-1 at 2399.88 m (Fig. 7), above several meters of fractured ooid–peloid mudstone–wackestone. In thin section, the bed contains clay and quartz silt, which are present both in peloids and their matrix. Carbonate grains are subrounded to subangular dark pellets or compound peloids with anastomosing, circumgranular fractures. Fenestral pores and circumgranular fractures are lined by fibrous dolomite cements similar to those in brecciated mudstones–wackestones. Larger fractures contain geopetal pellets and peloids similar to the matrix.

Stromatolite Framestones and Isopachous Laminites

In all three wells, very thin- to medium-laminated isopachous dolomite forms centimeter- to decimeter-thick conical, domal, and club-shaped stromatolites (Fig. 8). Stromatolite laminae are all highly regular and grew normal to irregular bed surfaces, including propagating the relief of grain-scale and bedform-scale roughness. The laminae have several textures: very thin, crinkly laminae (Fig. 8A); very thin, smooth laminae (Fig. 8B, C); and thin- to medium-bladed and columnar cement laminae (Fig. 8D). Laminae are typically couplets of very thin micritic or palisade cements and very thin, porous, grumelous (diffuse autochthonous micritic lumps up to 100 μm wide, *sensu* Turner et al. 2000), or micritic dolomite layers (Fig. 8E–G). In club-shaped stromatolites, the laminae are overhanging and consistent with at least 12 cm of synoptic relief (Fig. 8A). Domal, isopachous stromatolites with at least 6 cm of synoptic relief were gradational with the fenestral-laminite facies (Fig. 8B).

Grainstones filling synoptic relief between, or bound by, the stromatolites consist of well-sorted coarse to very coarse ooids and intraclasts (Fig. 8A), often with moldic pores of grains. Ooid nuclei are often very thin, platy moldic pores that are likely molds of isopachous stromatolite laminae. Grainstones have both current ripples and oscillation ripples. Anhydrite laths and centimeter-scale nodules replace stromatolites and grainstones.

Laminated and Cross-Bedded Packstones–Grainstones

All three wells contain very thin to thin cross-laminated dolomite grainstone beds (Fig. 9A, B) and nodular to wavy, thickly laminated and thinly bedded packstones (Fig. 9C). Grains are dominantly nondescript, recrystallized, very fine to fine peloids. Moldic pores preserve evidence of medium-grained to coarse-grained ooids and sometimes coarse-grained *Cloudina* or *Sinotubilites* fossils (Conway Morris et al. 1990; Amthor et al. 2003; Chen et al. 2008; Grotzinger and Al-Rawahi 2014) (Fig. 9A). Cross-laminae constitute centimeter-scale current ripples. Very thin, crinkly dolomite laminae similar to those in the stromatolite-framestone facies bind some cross-bedded grainstones (Fig. 9B). Laminated ooid–*Cloudina* packstones–grainstones are locally interbedded with centimeter- to decimeter-scale thrombolitic mounds. In Z-1, wavy, thick laminae and very thin beds of packstone–grainstone are separated by several-millimeters-thick undulating horizons of bladed marine cements (Fig. 9C). Often, fabric-destructive dolomitization of grainstones resulted in nearly massive texture with pale beige palimpsest laminae and beds. In one case, an interbedded packstone preserves evidence of saccate microfossils, possibly acritarchs (Butterfield and Grotzinger 2012), despite pervasive neomorphism (Fig. 9D, E).

Massive and Laminated Thrombolite Boundstones

Densely mottled and vuggy thrombolite boundstones form medium to very thick (up to 2 m thick) beds in Z-1 and form thin to medium beds in Y-2 and X-7 (Fig. 10A). In massive thrombolite boundstones, thrombolite mesoclots form millimeter- to centimeter-scale shrubby or reticulate mounds and decimeter-scale domes. The reticulate framework of many thrombolites is rimmed by clotted, dendritic microtexture similar to *Angulocellularia* (Mattes and Conway Morris 1990; Riding 1991) but is

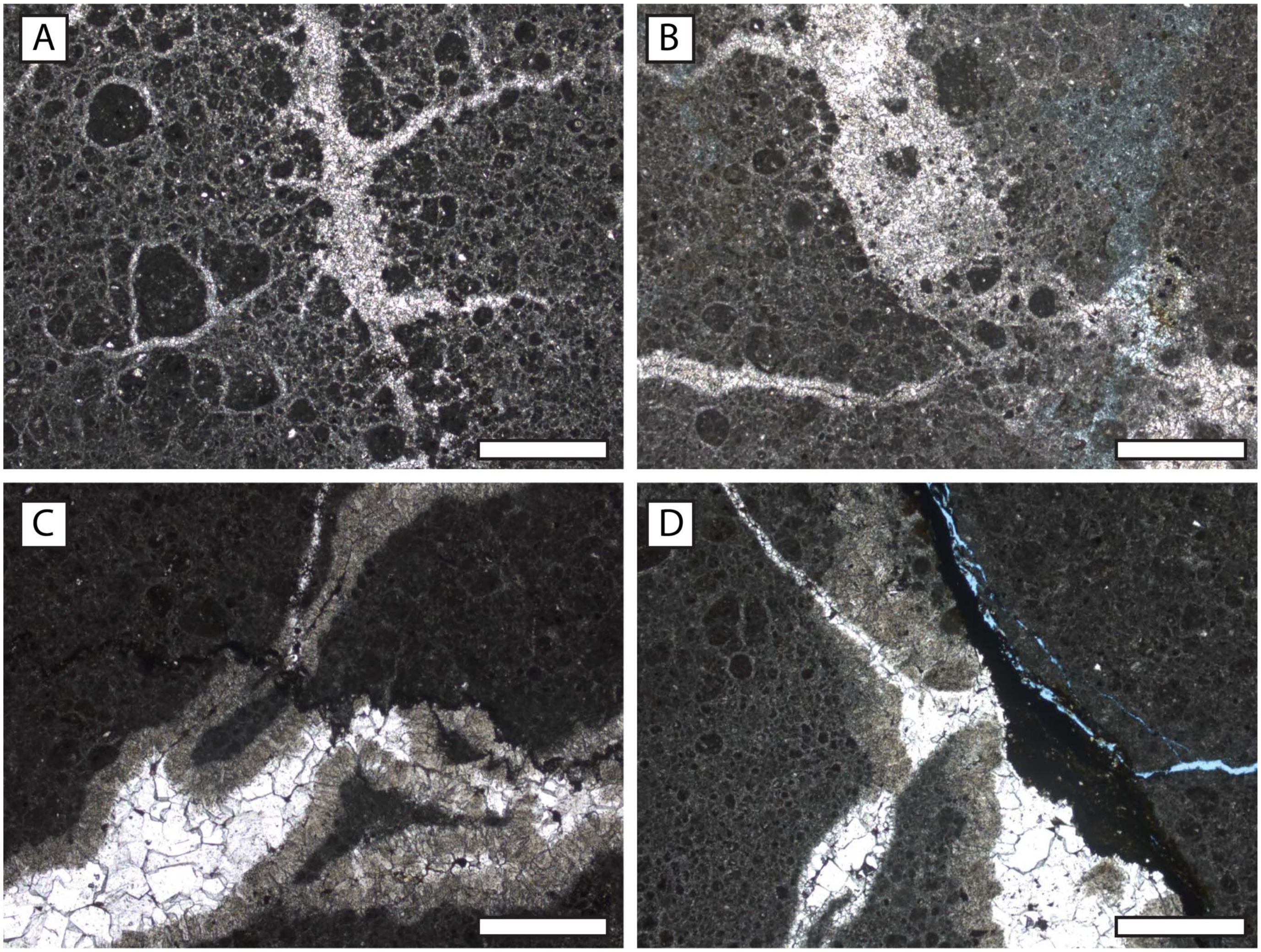

FIG. 7.—Silty peloid mudstone–packstone interpreted as a pseudomicrokarst, Z-1 2399.88 m. Scale bar is 500 µm in all photomicrographs. **A)** Anastomosing veins and circumgranular fractures around peloids. **B)** Poorly sorted peloidal geopetal fill in anastomosing fracture. **C**, **D)** Stylolites truncating anastomosing veins lined by fibrous dolomite cement.

typically heavily obscured by neomorphic dolomite. *Cloudina* shell fragments are recognizable in thrombolites, but, unlike younger Ediacaran-age carbonate stringers in the Ara Group (Amthor et al. 2003), *Namacalathus* fossils were not identified.

Thrombolite boundstones also form medium and thick beds with discontinuous, wavy, thick laminae in all three wells (Fig. 10B). Laminated thrombolite boundstone has feathery, dendritic mesoclot clusters emanating both upwards and downwards into centimeter-scale primary framework voids; these are frequently filled by micrite or fibrous marine cements. The laminated thrombolite boundstone lacks fenestral pores and has more discontinuous laminae than the fenestral-laminite boundstone facies.

Centimeter- to decimeter-scale thrombolitic mounds formed syndepositional relief filled by mudstones, wackestones, packstones, and grainstones. In these thrombolite framestones, featureless or poorly laminated peloid mudstones, wackestones, and packstones fill decimeter-scale cavities and channels between mounds. They are very thin to medium beds that are nodular or thickly laminated. Thrombolite framestones contain abundant *Cloudina* grains (Fig. 10C), and neomorphic nonplanar dolomite preserves dark grumelous microfossils (Turner et al. 2000), including chambered, *Renalcis*-like shrubs (Pratt 1984) (Fig. 10D).

Thrombolite-Intraclast Packstones–Rudstones

Variously matrix-rich intraclast packstone–rudstone facies are present as thin to medium beds in all wells. Intraclast grains are subspherical to tabular, coarse sand- to pebble-size mudstone and thrombolite rudstone fragments (Fig. 11). Thrombolite fragments are irregularly shaped and have irregular, feathery margins (Fig. 11A). The packstone matrix is silt- to sand-size peloids with quartz silt (Fig. 11B). Grains and pores are lined by isopachous marine cements.

Bedforms are not apparent in thrombolite-intraclast rudstones, but some beds are graded (Fig. 11C). Clasts are sometimes dissolved, leaving vuggy moldic pores with micritic dolomite envelopes or isopachous- or bladed-dolomite cements (Fig. 11D). Some clasts also have scalloped margins or micron-scale embayments interpreted as dissolved clast edges (Fig. 11A, D).

Dolomitic Siltstones

Very thin to medium beds of laminated and cross-bedded dolomitic siltstones and silty dolomite are greenish and include angular quartz silt, pyrite, or silt-size opaque spheroids (Fig. 12). Beds have stylolitic bases

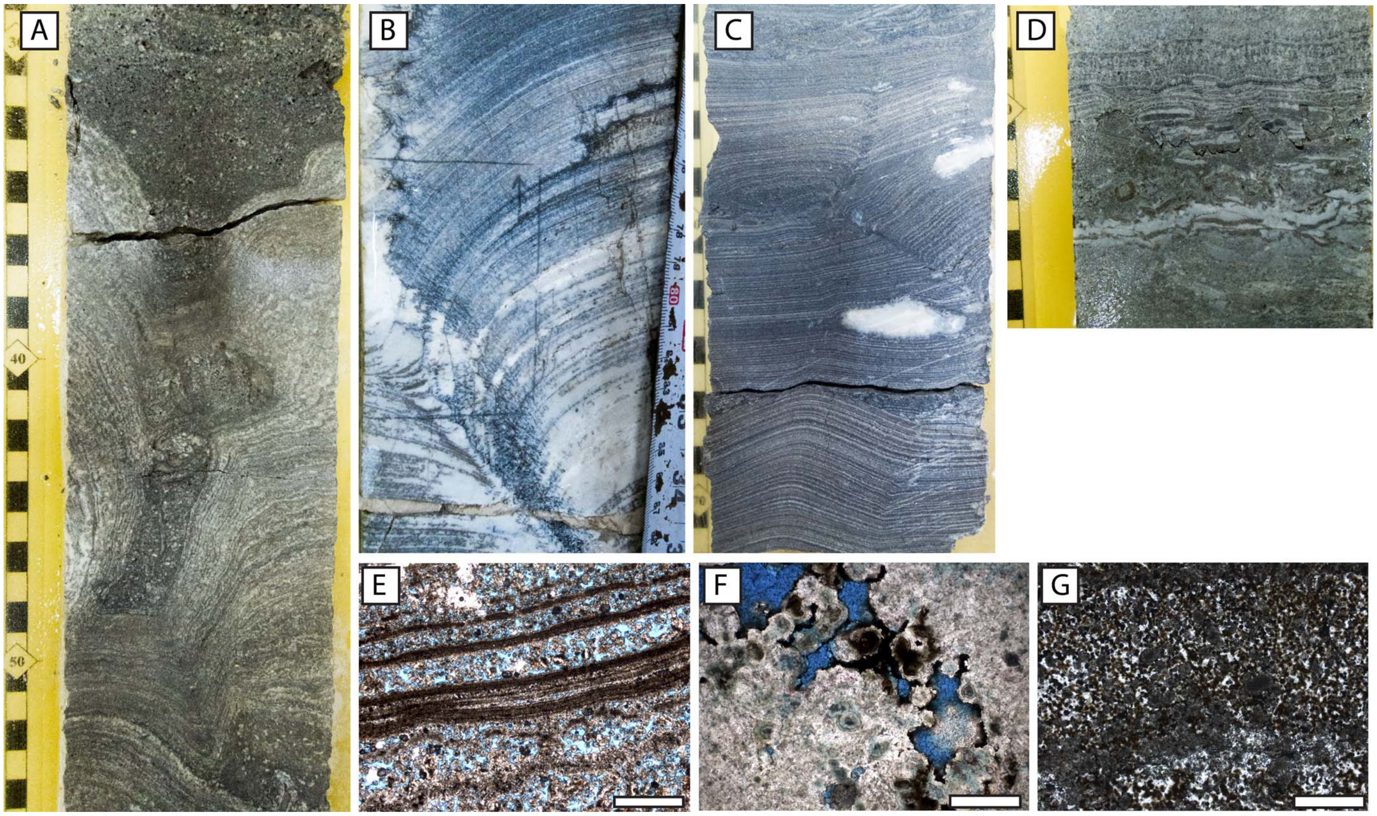

FIG. 8.—Stromatolites and isopachous laminites interpreted as high-energy subtidal precipitates. **A)** Club-shaped stromatolite framestone with crinkly laminae and ooid-intraclast grainstone between heads, X-7 3578.4 m. **B)** Domal stromatolite with isopachous laminae interfingering with fenestral laminite, X-7 3608.78 m. **C)** Isopachous laminite with anhydrite nodules replacing laminae before compaction, X-7 3576.6 m. **D)** Isopachous laminite with thick laminae composed of bladed cement nucleated on tabular intraclasts in packstone with stylolite, X-7 3580.2 m. **E)** Photomicrograph of alternating porous and microcrystalline dolomicrite couplets, scale bar is 500 μm, X-7 3576.57 m. **F)** Grumeaux and spheroidal dolomite in domal isopachous stromatolite, scale bar is 250 μm, X-7 3608.74 m. **G)** Grumeaux and micritic peloids in isopachous laminite, scale bar is 500 μm, Y-2 5299.42 m.

and stylolitic or gradational tops. In X-7, one such bed has ripple cross laminae and gently domed—possibly hummocky—cross laminae.

Clast-Supported Breccias

In X-7, matrix-poor angular intraclast breccias form thin to very thick, poorly defined beds and filled wedge-shaped solution-enlarged fractures with centimeter to decimeter apertures (Fig. 13). Clasts in these breccias are millimeter- to decimeter-size fine- to coarse-crystalline dolomite, which may retain broken synsedimentary laminae. Medium- and thick-bedded breccias are in some instances intercalated with very thin to thin beds of laminated or rippled dolomite silt and sand (Fig. 13C). Interparticle porosity is filled by halite or anhydrite (Fig. 13D).

These angular, clast-supported units are sometimes difficult to distinguish from matrix-poor thrombolitic rudstones. They are differentiated by greater clast angularity than thrombolitic intraclast rudstones and by their presence filling subvertical fractures in surrounding strata.

Paragenesis

The diagenetic overprint in all three wells is pervasive, and rock fabrics reflect processes that started contemporaneously with deposition and continued for several kilometers of burial. Dolomite is the predominant mineral in all samples, with subordinate calcite, siliciclastic clay, quartz, pyrite, anhydrite, halite, and bitumen. The BAC shelf-margin paragenesis as observed in the three wells is summarized in Figure 14.

Dolomite fabrics include both clear and inclusion-rich microtextures that are micritic, fibrous, bladed, nonplanar sparry, and subhedral and euhedral planar. Cloudy, neomorphic, nonplanar to planar subhedral dolomite overprints nearly all samples (Fig. 4E, F). In some cases, primary depositional fabrics are preserved as dark mimetic dolomicrite (Figs. 4E, F, 15C). These include laminae in boundstones, oncoids, and pisoids. In fabric-destructive neomorphic dolomite, diffuse white-card petrography sometimes revealed primary peloidal or calcimicrobial microtextures (Fig. 10J). However, most depositional rock textures are preserved in planar subhedral dolomite, with only palimpsest primary rock fabrics highlighted by pores that are fenestral (e.g., laminated boundstones), intergranular (e.g., breccia clasts), intragranular (e.g., *Cloudina* fossils, ooids), intercrystalline (e.g., aragonite cements), and moldic. Most of these pores remain open or are filled by halite, but in Y-2 some are filled by later, clear planar or poikilitic calcite, dolomite, and anhydrite (Figs. 11B, 15E).

Fibrous and bladed cloudy dolomite form isopachous and botryoidal cements (Fig. 15A). These line early diagenetic fractures in nodular, laminated, and brecciated mudstones–wackestones (Fig. 6D), thrombolitic intraclast rudstones (Fig. 11B, D), and angular clast-supported breccias (Fig. 13E). Planar dolomite, which is interpreted to have replaced aragonite primary marine cements, was identified by columnar pore networks (Fig. 13F), by dolomicrite laminae that highlighted square-tipped (orthorhombic) crystal shapes (Fig. 4E), and by botryoidal masses of porous dolomite pseudospar (Fig. 15B).

Anhydrite is mostly a replacive phase (Fig. 15F), although some mudstones have anhydrite nodules that formed before compaction and brecciation

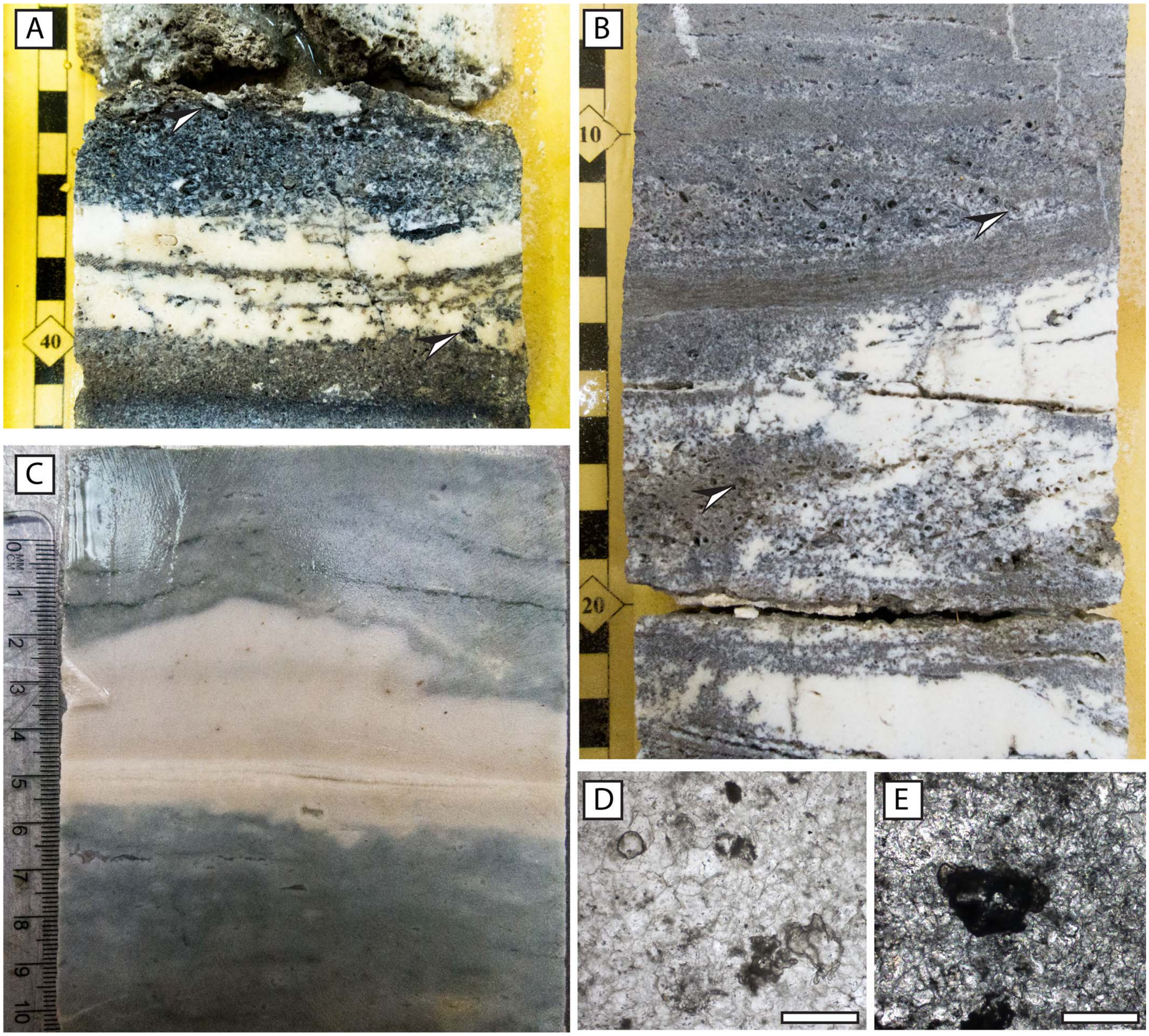

FIG. 9.—Laminated and cross-bedded packstones–grainstones interpreted as open-platform sand shoals. **A)** Cross-bedded ooid–*Cloudina* (arrows) grainstone with moldic pores, X-7 3595.4 m. **B)** Cross-bedded ooid–*Cloudina* grainstone with intercalated crinkly laminated boundstone, X-7 3596.2 m. **C)** Nodular and wavy-bedded packstone and grainstone, Z-1 2768.3 m. **D, E)** Saccate microfossils in packstones, 200 μm scale, Z-1 2769.19 m.

(Figs. 6B, 8C). Replacive anhydrite forms euhedral blades that abruptly cut mimetic dolomicrite laminae or overgrow allochems. This relationship between an early generation of aphanitic anhydrite that replaces evaporitic gypsum nodules and a later generation of euhedral laths and blades that replace dolomite was also observed in carbonate stringers by Schröder et al. (2003). Halite is a replacive phase and commonly fills intercrystalline microporosity associated with solution-enlarged fractures and dolomitized intraclasts, or as poikilitic void-filling cements (Fig. 15G). Halite cementation before pressure solution or bitumen emplacement, as observed in A1C and A2C stringers (Schoenherr et al. 2009), is not apparent in the BAC cores from the Birba Platform margin.

Some micropores are lined by bitumen that highlights primary fabrics in core slabs. Pore-lining bitumen may have blocked further dolomite cement precipitation during burial, preserving early diagenetic pore structures (Figs. 8F, 15H). More commonly, however, bitumen lines secondary pores in dissolved dolomite (Figs. 13E, 15I, 16A), indicating that carbonate dissolution predated or was coincident with hydrocarbon migration (Schoenherr et al. 2009).

Compressional fractures produced breccias with fitted clasts (crackle breccias) and with loosely fitted and rotated fragments (mosaic breccias) (Fig. 16) (Loucks 1999). In particular, core intervals with thick packages of pisoid rudstone and void-filling cement boundstone are typically pervasively fractured into mosaic breccias. Some mosaic-breccia clasts occur in solution-enlarged fractures and are crosscut by stylolites, indicating that compressional fracturing predated aqueous dissolution and pressure solution. Fractures commonly are filled by bitumen and halite.

In some notable cases, fracturing and brecciation also predate marine cementation and later dolomitization. For example, aragonite-fringing cements grew on dolomitized clasts in a grike in X-7 (Fig. 15J, K). Chaotic

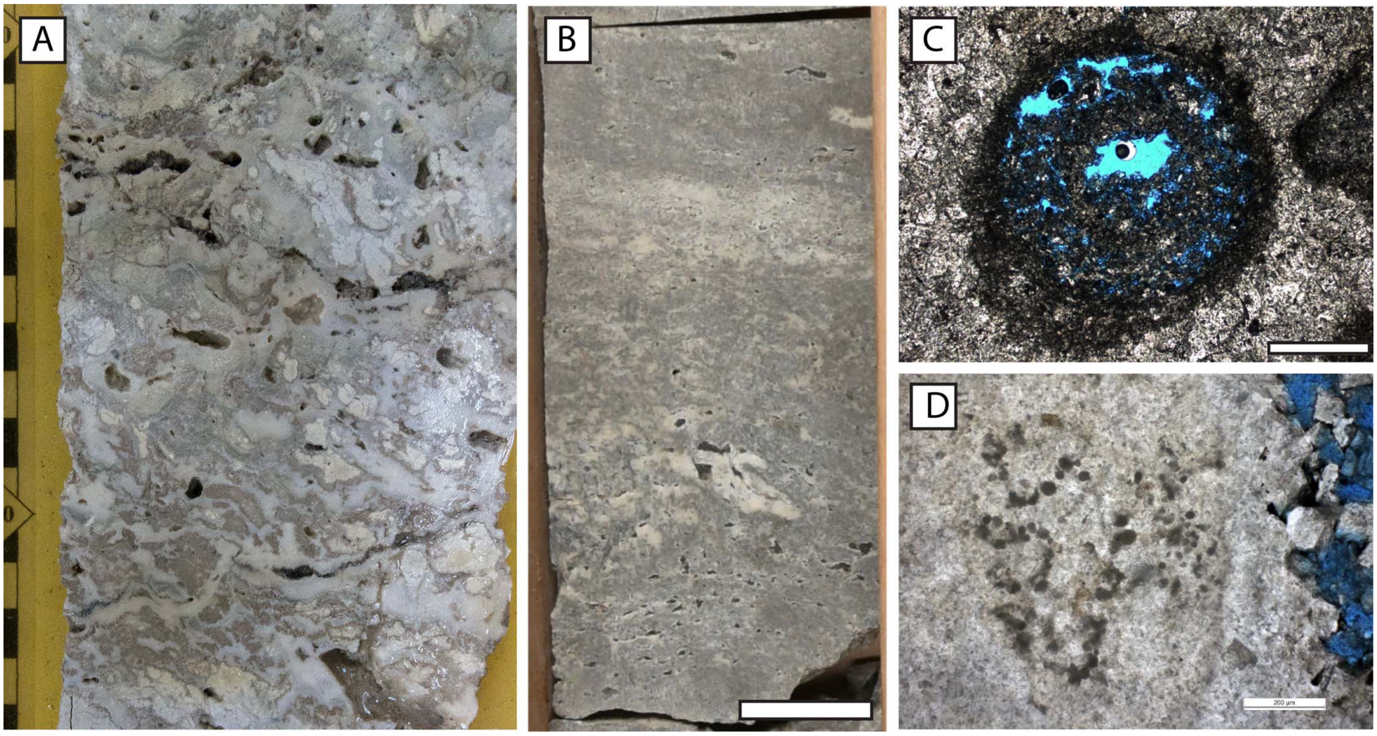

FIG. 10.—Thrombolite boundstones interpreted as patch and shelf-margin reefs. **A)** Massive thrombolite with vermiform dendrites and micritic vug-filling cements, X-7 3587.7 m. **B)** Poorly laminated thrombolite, 4 cm scale, Z-1 2460.77 m. **C)** *Cloudina* microfossils, 500 µm scale, Z-1 2624.1 m. **D)** *Renalcis*-like dendritic calcimicrobe in framestone matrix, X-7 3633.29 m.

clast-supported breccias were typified by moldic porosity (Fig. 15L) and fabric-destructive dolomitization, which indicates that dissolution and compressional-brecciation processes were nearly coincident. Importantly, fabric development of all breccias predated deep-burial diagenetic features including stylolite formation, rhombic dolomite cementation, poikilitic calcite and anhydrite cementation, bladed-anhydrite replacement, and bitumen emplacement.

Chemical Images

Manganese and iron are soluble as Mn^{2+} or Fe^{2+}, but Mn(IV) oxides are reduced at suboxic conditions while Fe(III) oxides are reduced at more fully anoxic conditions. As such, carbonates bearing neither metal formed in oxic conditions, carbonates bearing Mn but not Fe formed in suboxic conditions, and carbonates bearing Fe formed under fully reducing conditions. Cathodoluminescence microscopy has long been used to relate paragenesis and cement stratigraphy to aquifer geochemical conditions because Mn causes carbonates to luminesce and Fe quenches this effect, resulting in the brightest cathodoluminescence corresponding to suboxic conditions (Grover and Read 1983; Barnaby and Rimstidt 1989).

XRF chemical images similarly reveal that the earliest diagenetic fabrics—mimetic and nonplanar dolomite—precipitated in the presence of soluble Mn and/or Fe (Fig. 17; Table 1). Neomorphic dolomite in mudstones, laminites, and grainstones is consistently enriched in Mn and in some cases has low Fe (e.g., a mudstone intraclast in Fig. 17A), which suggests that dolomitization at least began under suboxic conditions. However, neomorphosed dolomite is Fe-rich (e.g., peloid packstone matrix in Fig. 17A, mudstone in Fig. 17B, and pedogenic silty dolomite in Fig. 17C), which suggests that some dolomitization occurred by fully anoxic diagenetic fluids. Intraclasts in thrombolitic-intraclast rudstones are observed to have been dolomitized before brecciation in more Mn-rich fluids than those in chaotic clast-supported breccias, which are composed of lower-Mn fabric-destructive dolomite (Fig. 17D).

Mimetic dolomicrite and micritic envelopes on clasts are consistently enriched in Fe, and marine and burial cements are variously enriched in Mn and Fe. Notably, many of the latest generations of cement have the highest Mn concentrations (Fig. 17A–D; Table 1). This relationship indicates that later diagenetic fluids—in some cases, following mosaic-breccia development, solution enlargement of fractures and pores, and formation of chaotic breccias—were more closely related to surficial, oxidizing fluids than to those that formed earlier marine-diagenetic textures. This is interpreted to be evidence for development of suboxic groundwater or burial fluids in relatively near-surface environments.

DISCUSSION

Depositional Model

Seismic observations show that the BAC was broad and flat-lying across the Birba Platform interior, and that the platform margin abruptly deepens eastward to the center of the SOSB (Figs. 2, 18A). A depositional model for the steep-rimmed carbonate-platform margin (Fig. 18) was constructed from sediment composition, sedimentary structures, observed interfingering of facies, and vertical stacking patterns (Fig. 3 and Supplemental Information).

Using the depositional model (Fig. 18B), beds are organized into meter-scale cycle sets interpreted from distal facies disconformably overlying proximal facies, which in turn patterned 10–30-m-thick packages interpreted as transgressive–regressive sequences. Vertical successions of strata are interpreted in detail for each core in the Supplemental Information. Although cycle sets are composed of smaller packages of laterally contiguous cycles, variability in their thickness, bathymetry, and extent makes distinguishing correlatable bounding surfaces or identification

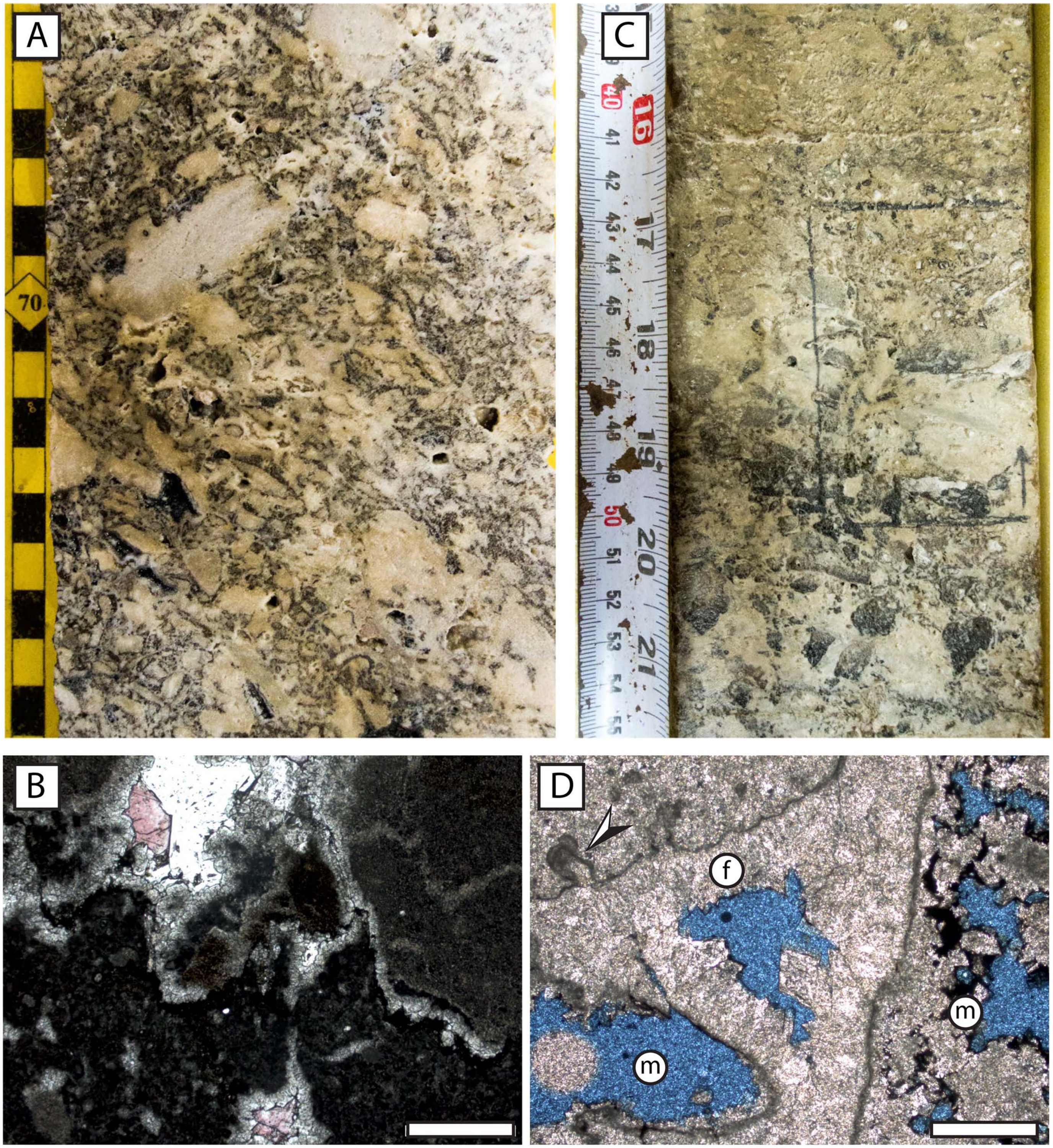

FIG. 11.—Thrombolite-intraclast rudstones interpreted as debris shed from patch reefs. **A)** Intraclast rudstone with tabular and elliptical clasts that have feathered, irregular margins, X-7 3630.7 m. **B)** Thin section of intraclast packstone, 500 μm scale, Y-2 5303.73 m. **C)** Graded, clast-dominated intraclast packstone–rudstone with bitumen-stained thrombolite intraclasts and tabular mudstone intraclasts, X-7 3628.47 m. **D)** Thin section of intraclast rudstone in Part C, showing molds of intraclasts (m) and embayed clast margins (arrow) cemented by fibrous marine cement (f). Scale is the same as Part B.

of deterministic cycles challenging (Kerans and Tinker 1997). Thus, we did not attempt to delineate these smaller-scale cycles or distinguish between their deposition during regressive or transgressive regimes (Rivers and Dalrymple 2025). However, vertical trends in cycle-set thicknesses provide an indicator of accommodation change; sequences are characterized by thick or thickening basal-cycle sets (transgressive) overlain by progressively thinner regressive-cycle sets, diagnostic of decreasing accommodation (Goldhammer et al. 1990). Several of these transgressive–regressive

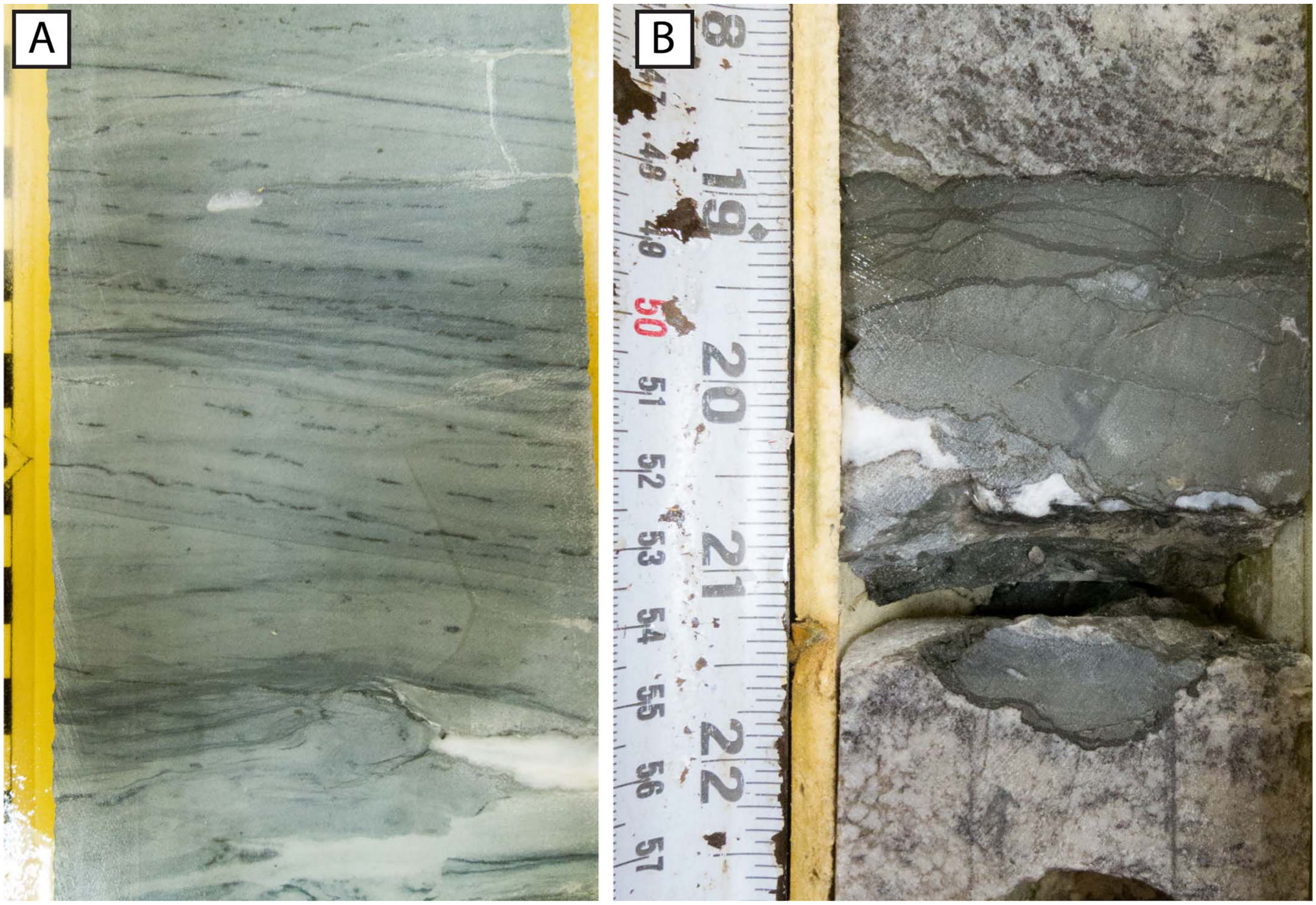

FIG. 12.—Dolomitic siltstones interpreted as subtidal volcanic ashes. **A)** Cross-bedded siltstone with climbing ripples or hummocky cross stratification, and convolute bedding with anhydrite nodules, X-7 3618.1 m. **B)** Stylolitic siltstone with anhydrite nodules, Y-2 5306.5 m.

sequences were bounded by cored-exposure surfaces associated with diagnostic paleokarst features (Fig. 19).

Nodular to laminated, peloidal mudstones to packstones with evaporite nodules or molds are interpreted as inner-shelf, low-energy, subtidal evaporitic lagoonal facies. Evaporite nodules and molds are common, but laminated carbonate–evaporite couplets, like those seen in younger Ara stringers (Schröder et al. 2003; Grotzinger and Al-Rawahi 2014), are not observed in the BAC shelf-margin cores. Lagoonal mudstones to packstones are composed of mud and peloids, and they lack ooids or *Cloudina* fossils, which are found in other grainy subtidal facies. Wavy subhorizontal fractures filled with bladed dolomite cements in lagoonal peloid packstones are interpreted as fenestrae or sheet cracks, and laminated or bladed cements in these pores contributed to incipient auto-brecciation of mudstones (e.g., Fig. 6D), forming diagenetic rudstones (Mazzullo and Birdwell 1989). These mudstone and packstone facies interfinger with thick evaporite strata west of the Birba Platform margin, comprising sediments in the intrashelf basin between the Birba and Harweel areas (Figs. 2G, 18A) (Mattes and Conway Morris 1990; Al-Siyabi 2005).

Quartz-rich dolomitic siltstones and silty dolomites are interpreted to be volcanic-ash airfall and distal windblown sediments (Bowring et al. 2007). These are found predominantly in association with the subtidal lagoonal facies, where wavy bedding and cross stratification indicate reworking in a shallow marine environment. While the platform interior was largely a low-energy, protected environment, domed (possibly hummocky) cross stratification seen in X-7 is interpreted to have formed by waning oscillatory flow (Southard et al. 1990), where sporadic storm-wave energy impacted subtidal lagoonal water depths (Mattes and Conway Morris 1990).

Pisoid–oncoid rudstones and fenestral laminites are lithofacies associated with brecciation and intense cementation. These facies are interpreted as intertidal microbial flats near where auto-brecciated tepee structures with prism cracks and sheet cracks formed in supratidal borders and mounds (Fischer 1964; Kendall 1969; Assereto and Kendall 1977; Assereto and Folk 1980). Incipient tepees formed where centimeter-scale irregular fenestral pores lined by isopachous cements created *in situ* intraclasts. Botryoidal, laminated, isopachous, and festoon cements form void-filling cement boundstones in beds up to 40 cm thick, which are interpreted to be pendant cements and flowstones that filled sheet cracks in large supratidal tepee structures (Assereto and Folk 1980). Fenestral laminites that form 2–6-cm-tall crinkly stromatolites are interpreted to have formed in the shallowest subtidal environments with enough accommodation for the synoptic relief of the stromatolites. These microbial tidal flats and closely associated supratidal tepee-pisolite complexes represent the geomorphically highest region on the Birba Platform, which created a hydrographic barrier separating outer-shelf subtidal facies from evaporitic, subtidal back-barrier lagoonal facies (Mattes and Conway Morris 1990; Amthor et al. 2005).

The cross-bedded ooid–intraclast packstone–grainstone facies was deposited in close relation to isopachous stromatolites and laminites. Uniform, isopachous stromatolite laminae likely formed by *in situ* encrustation of the seafloor (Pope et al. 2000), whereas larger stromatolite framestones have

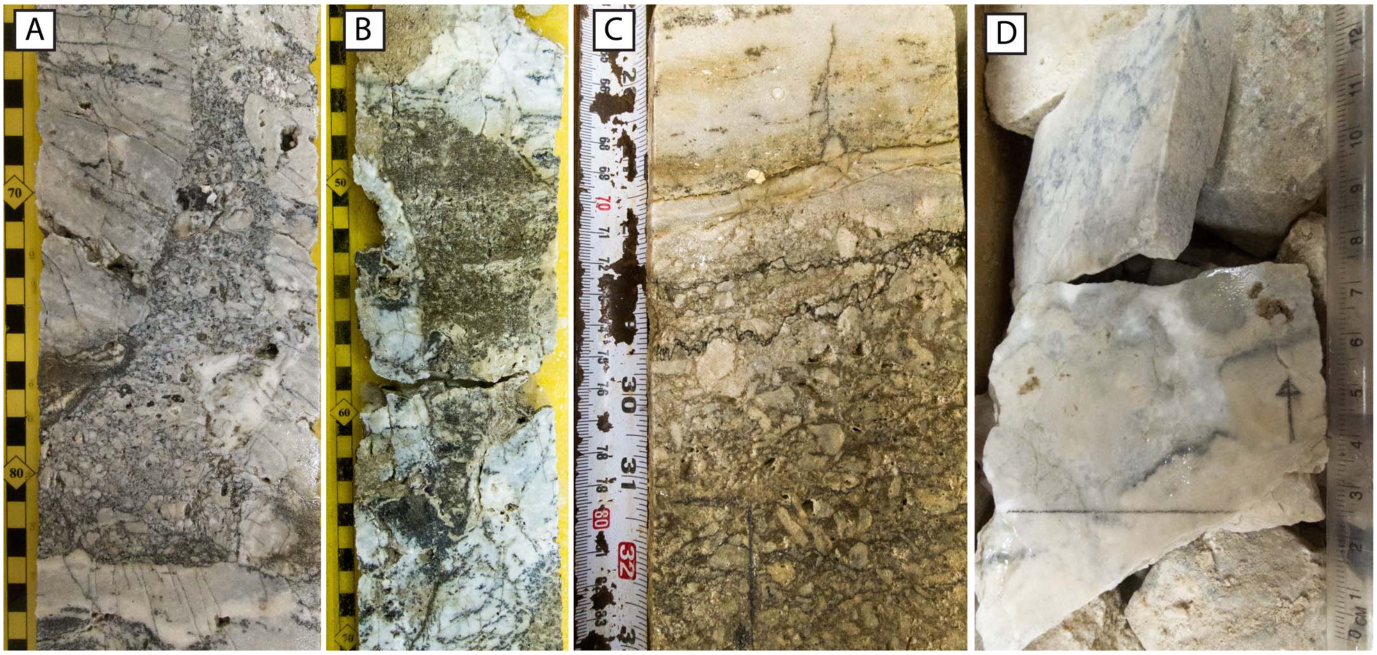

FIG. 13.—Clast-supported breccias interpreted as grike fills and paleocave-collapse breccias. **A)** Solution-enlarged fracture in laminated wackestone with breccia fill, X-7 3623.7 m. **B)** Solution-enlarged fracture in laminated mudstone with poorly bedded breccia fill, X-7 3620.5 m. **C)** Clast-supported breccia overlain by rippled dolomite silt, X-7 3619.8 m. **D)** Anhydrite-cemented breccia with dark geopetal coatings on clast tops, Z-1 2624.34 m.

crinkly laminae with grains and peloids that likely formed by microbial trapping and binding or *in situ* microbial precipitation of peloids (Pope et al. 2000; Reid et al. 2000). In modern high-energy subtidal environments, stromatolites form where aragonite crusts stabilize bedforms (e.g., Dravis 1983), but Precambrian hardgrounds may have lacked diagnostic encrusting and boring fauna. These facies are similarly interpreted to be high-energy subtidal shoals on which precipitated crusts provided a stable substrate for additional isopachous-cement laminae to precipitate from seawater. Symmetric wave ripples are only seen cemented by and interbedded with isopachous laminites, suggesting that the laminites co-occupied a subtidal upper-shoreface position with high carbonate-precipitation rates and fair-weather wave activity. The isopachous stromatolite laminae grade directly into fenestral laminites (Fig. 8B) and are interbedded with packstone–grainstones (Fig. 9B), which places this facies in between the up-dip (platform-ward) microbial flats and the down-dip (margin-ward) open-platform shoals.

Unidirectionally cross-laminated grainstones interfinger with both crinkly isopachous laminae like those in the club-shaped isopachous laminated stromatolites (Fig. 9B), and with small thrombolitic mounds. Grains include sand-size intraclasts, ooids, and *Cloudina* fossils. We interpret this facies association to be open-platform shoals between upper-shoreface stromatolite patch reefs and outer-shelf, lower-energy thrombolite mounds. Some grainstones may represent tidal-channel or tidal-inlet deposits cutting through the supratidal barrier and prograding lagoonward during transgressions, like dip-oriented tidal channels in Permian ramp-crest settings that are succeeded by margin-parallel shoal complexes on the outer ramp during highstands (Barnaby and Ward 2007; Rush 2022), or by modern stromatolitic tidal-bar complexes on the platform sides of Pleistocene antecedent barrier islands (Dravis 1983; Dill et al. 1986; Rush and Rankey 2017; Cruz and Eberli 2019). The BAC grainstone and stromatolite facies association is present in transgressive intervals (Supplemental Information), consistent with either position. Distinguishing tidal complexes from margin-parallel shoals requires lateral facies geometries not apparent in vertical core sections. In core, grainstones interfinger with small thrombolite mounds like those on the outer BAC shelf margin (see next paragraph) and with isopachous stromatolites that pass into barrier-complex fenestral laminites (Fig. 8B), but they are not observed to interfinger with evaporitic lagoonal facies; this constrains most grainstone deposition to a position outboard of the barrier.

Laminated and massive thrombolite framestones and boundstones are interpreted as outer-shelf and shelf-margin reef facies (Fig. 10), which shed limited amounts of intraclast debris basinward (Fig. 11). The thrombolitic facies are more mud-rich and lack bedforms, indicating that they formed in a low-energy sub-wave-base environment. The reticulate framework of thrombolite boundstones with pores outlined by clotted, dendritic microstructure has been interpreted as a calcimicrobial texture formed by physical disruption of the benthic community (Kennard and James 1986; Mattes and Conway Morris 1990; Cantine et al. 2020). Mud-rich thrombolite mounds and framestones represent small (< 10 cm high) patch reefs that coalesced into massive thrombolite boundstones and became increasingly laminated as the mound or patch reef aggraded and then developed lateral progradational growth.

Thrombolite intraclast rudstones—sometimes graded—are interpreted as reef-talus and gravity-flow deposits composed of irregular thrombolite intraclasts, *Cloudina* fossils, and mud shed off reef mounds and possibly downslope. Slope facies deposited below the shelf margin are not well represented in the BAC shelf-margin cores, especially compared to the widespread presence of slope breccias in transgressive sequence tracts near the base of A2-age carbonate stringers (Grotzinger and Al-Rawahi 2014).

Karst Overprinting

Two lithofacies are not interpreted as depositional: the angular-clast-supported breccias and the peloid mudstone–packstone.

Angular-clast-supported breccias are interpreted as cave-collapse breccias. In peritidal settings, however, syndepositional and diagenetic breccia fabrics are commonly gradational. Supratidal tepee-pisolite facies experience syndepositional brecciation from sheet-crack development, followed by vadose diagenetic overprinting during exposure, making discrimination challenging (Table 2). Nonetheless, several criteria indicate a postdepositional collapse origin for the angular-clast-supported breccias. First, breccia clasts have pervasive meteoric diagenetic textures including moldic porosity (Fig. 15L) and embayed margins, and interparticle pores

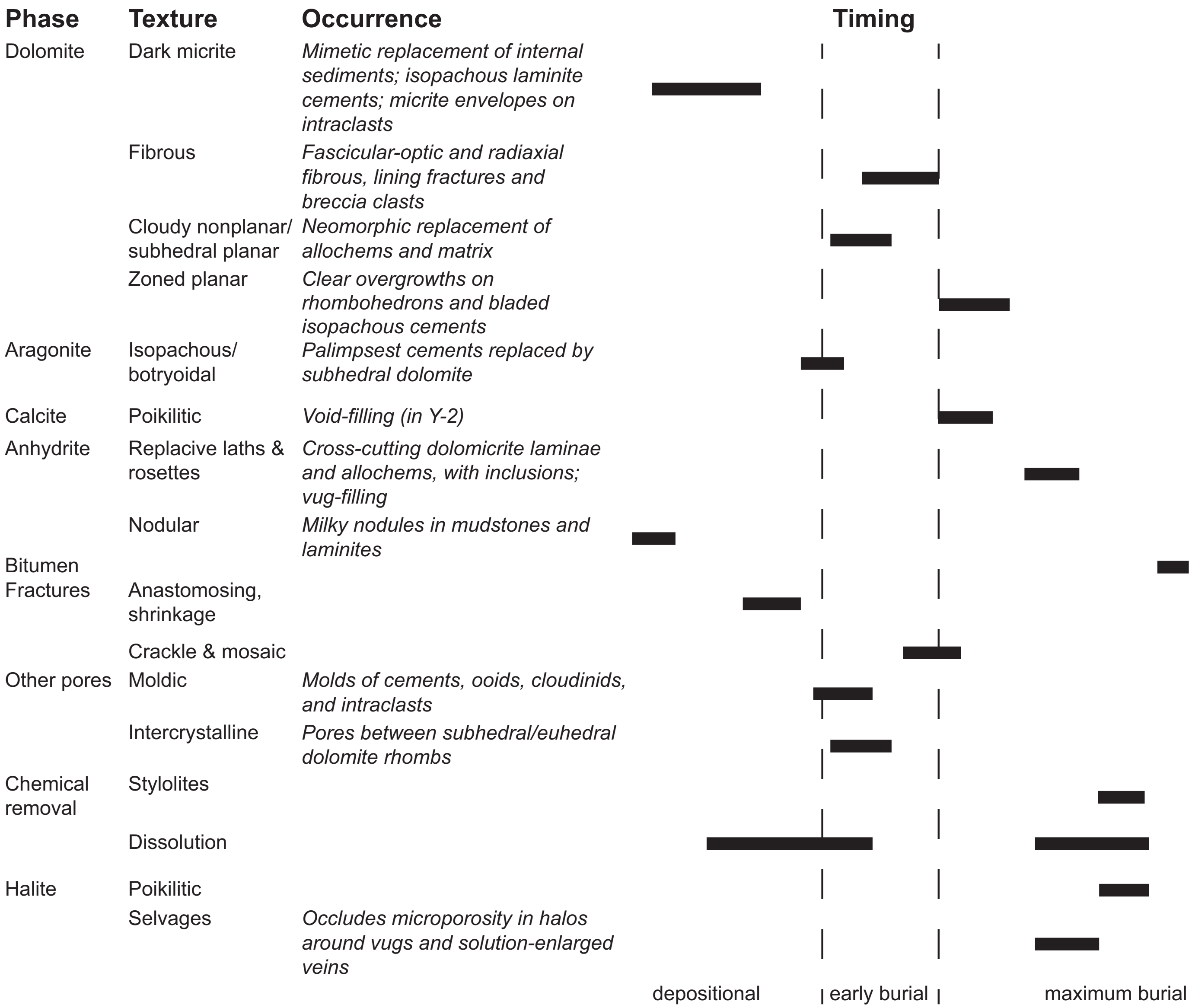

FIG. 14.—Paragenetic sequence of minerals and diagenetic features.

contain pendant cements and geopetal fills (Fig. 15J–L) indicative of vadose conditions. Second, the clast-supported breccias exist alongside crackle and mosaic breccias (Fig. 16), representing a continuum from *in situ* fracturing through rotated and collapsed clasts. Presence of these breccias in the core is strongly associated with compactional diagenetic features such as centimeter- to meter-scale fracture networks and centimeter-scale stylolites, and they are observed filling solution-enlarged fractures (grikes) with at least centimeter- to decimeter-scale apertures. This relationship is particularly diagnostic where compressional fracturing predated aqueous dissolution and pressure solution, as indicated by the presence of mosaic-breccia clasts in grikes and being crosscut by stylolites. Third, thin beds of laminated dolomite silt and sand associated with the breccias (Fig. 13C) may represent local sourcing of weathered, disaggregated host rock or reworking of internal sediments in pores before complete collapse (Rivers and Kaczmarek 2020). Fabric development of all breccias predated deep-burial diagenetic features including stylolite formation, rhombic dolomite cementation, and bitumen emplacement.

By contrast, thrombolitic intraclast rudstones in subtidal shelf-margin facies are more readily distinguished as depositional by the presence of marine allochems in a wackestone–packstone matrix, isopachous marine cements, graded beds, and interbedding with thrombolite boundstones. In thrombolitic rudstones with meteoric diagenetic overprint, such as moldic porosity and embayed clast margins, the leaching is superimposed on depositional and earliest-marine diagenetic fabrics.

Nearly all breccias are anhydrite- or halite-cemented but otherwise lack matrix material. Although a key diagnostic indicator of paleocave-collapse breccias are polymictic clasts and siliciclastic-rich sieved matrix (Kerans 1993; Loucks 1999), these are not observed; their absence is likely due to a lack of heterolithic overburden during karst development and the limited vertical extent of grikes and cave networks. This absence of geopetal siliciclastic matrix in the BAC stands in contrast to those observed at the Nafun–Ara unconformity in the northern Oman outcrop (Bergmann et al. 2025), where there was continent-derived siliciclastic material during basal-Birba time (Bergmann 2013; Gómez-Pérez et al. 2024a).

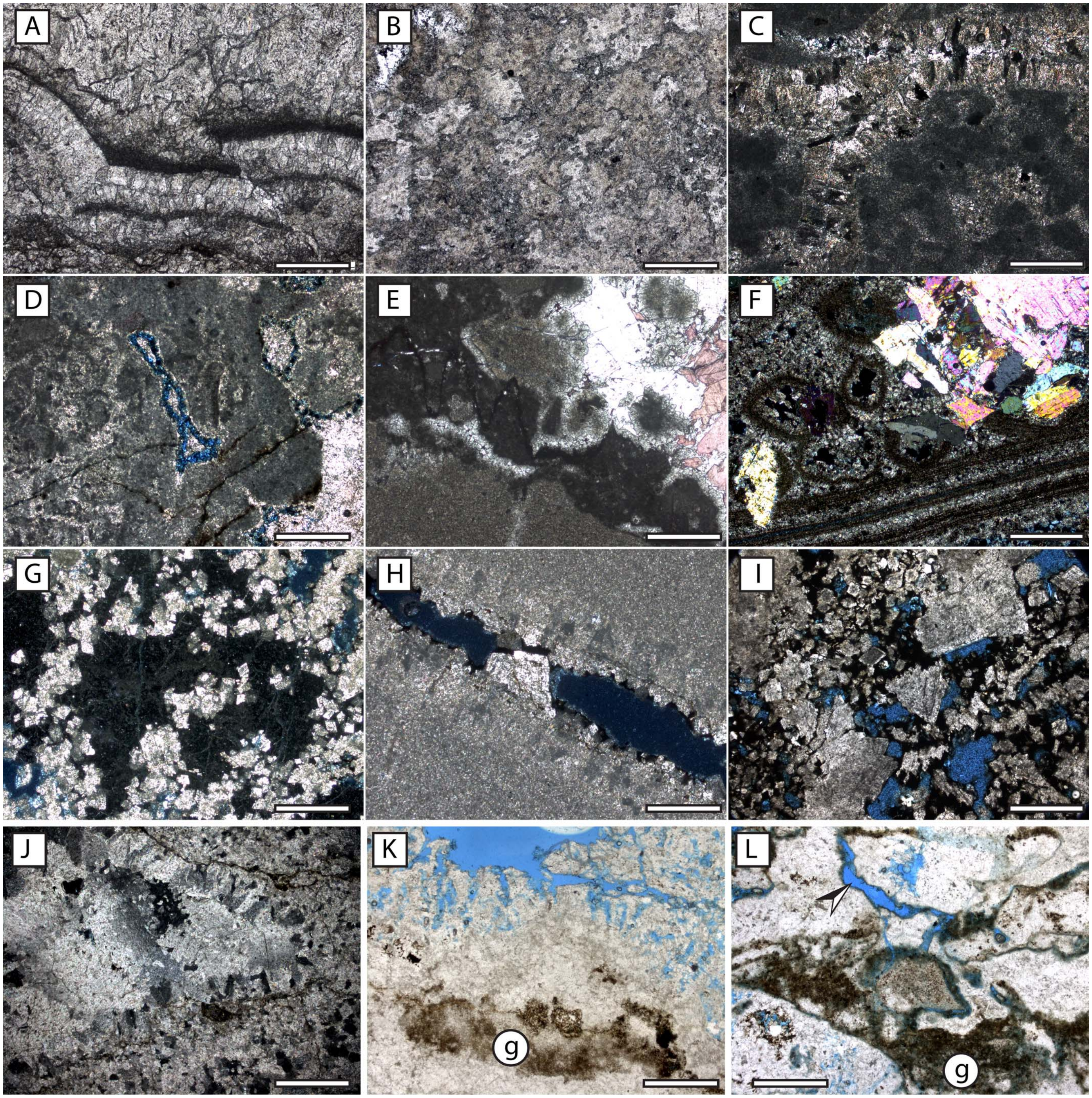

FIG. 15.—Microtextures and crosscutting relationships. Scale bar for all images is 500 μm. **A)** Bladed-dolomite cements in a sheet crack with geopetal micrite, fractured with a small reverse offset, Z-1 2774.37 m. **B)** Nonplanar dolomite pseudospar replacing fibrous cement in a sheet crack, X-7 3587.94 m. **C)** Fibrous dolomite cements on shrinkage cracks in fenestral peloid packstone, Z-1 2401.64 m. **D)** Leached, tepee-brecciated fenestral packstone with moldic pores of isopachous cements, X-7 3593.59 m. **E)** Mudstone intraclasts and peloid-packstone matrix cemented by anhydrite and calcite (stained) before stylolitization, Y-2 5303.73 m. **F)** Anhydrite replacing isopachous laminite with ooid grainstone, X-7 3576.57 m. **G)** Poikilitic halite overgrowing euhedral planar dolomite that replaced a thrombolite intraclast, X-7 3627.47 m. **H)** Bladed cements on shrinkage fracture in brecciated lagoonal mudstone, X-7 3616.64 m. Fracture is lined by bitumen. **I)** Euhedral saddle dolomite corroded during bitumen emplacement in mosaic breccia, X-7 3633.47 m. **J)** Bladed dolomite cements between breccia clasts in grike, X-7 3623.7 m. **K)** Columnar cements replaced by dolomite on clasts and geopetal peloidal silt (g) in grike, X-7 3620.5 m. **L)** Moldic pores of pendant cements (arrow) and geopetal peloidal silt (g) in grike, X-7 3620.5 m.

Despite the prevalence of anhydrite and halite plugging of pores, the clast-supported breccias were largely not interpreted as the result of evaporite dissolution and collapse. Several lines of evidence argue against evaporite dissolution as the primary brecciation mechanism. First, the breccias are in barrier facies (tepee-pisolite complexes and fenestral laminites) where bedded evaporites were not deposited, rather than in back-barrier lagoonal facies where anhydrite nodules appear as syndepositional structures. Bedded evaporites have not been cored along

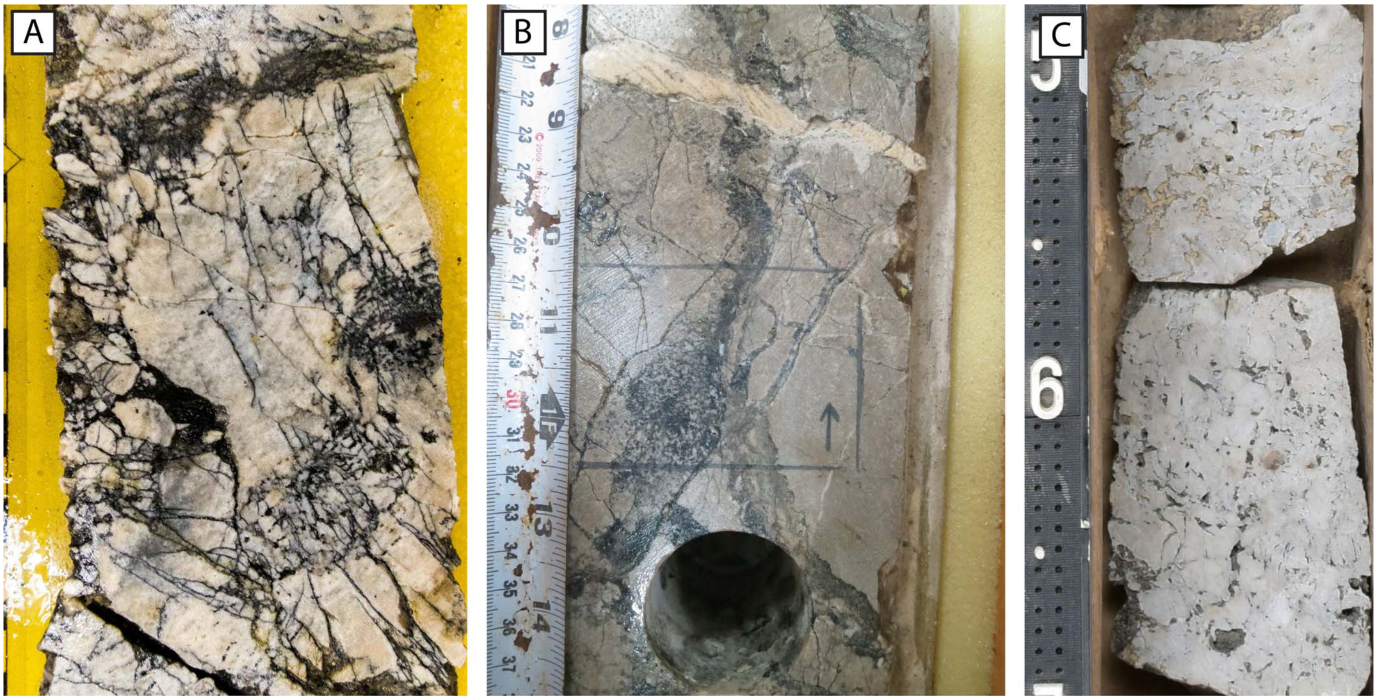

FIG. 16.—Crackle and mosaic breccias formed by physical compaction. **A)** Mosaic-brecciated wackestone, X-7 3624.7 m. **B)** Crackle breccia with solution-enlarged fractures, X-7 3633.29 m. **C)** Mosaic-brecciated mudstone with solution-enlarged fracture porosity, Z-1 2401.4 m.

the steep eastern shelf margin of the BAC. Thin-bedded evaporites are present in A2E-age strata west of the shelf margin, in Shamah-1, and other wells in the central Birba Cluster. These evaporite strata thicken westward into the platform-interior basin between the Birba and Harweel structural highs (Fig. 18A). Second, the breccias are monomictic, composed entirely of dolomite clasts. In both Birba and Harweel stringer carbonates encased in these evaporites, evaporite collapse associated with the carbonate–evaporite transition appears as polymictic breccias composed of both anhydrite and dolomite clasts (Schröder et al. 2003, 2005; Grotzinger and Al-Rawahi 2014). These evaporite-collapse breccias occur in deep subtidal settings and are associated with the freshening of the platform interior and initiation of carbonate deposition at the base of sequences, and are sometimes reworked in sediment-gravity-flow deposits (Schröder et al. 2005; Grotzinger and Al-Rawahi 2014). Thus, the brecciated fenestral laminites in the BAC formed in a different, geomorphically higher, and less evaporitic setting than evaporite-collapse breccias in the stringers. The stratigraphic position of breccias is also diagnostic: they are best developed below sequence boundaries, whereas evaporite-collapse breccias in Ara stringers are associated with flooding surfaces where normal salinity seawater dissolved underlying lowstand evaporites (Schröder et al. 2003). Third, anhydrite and halite are generally cements plugging pores of breccia clasts, not clasts or molds of clasts, indicating that evaporites precipitated after brecciation rather than dissolution causing it. Some dissolution of evaporite nodules may have occurred in intertidal fenestral facies during transgression and invasion of normal-salinity seawater at the basinal (eastern) edge of more evaporitic back-barrier lagoonal facies (Kendall 1969), manifesting as moldic pores in some cases associated with incipient, enterolithic brecciation after evaporites formed from shallow hypersaline groundwaters (Fig. 5). Finally, carbonate-dissolution features observed associated with the breccias, such as solution-enlarged fractures, grikes, and embayed clast margins or moldic pores, are expected from karst processes but not from evaporite dissolution driven by normal-salinity seawater.

A fault-related origin for clast-supported breccias is precluded on the basis of the absence of preferred clast-rotation directions and other, mainly paragenetic, criteria (Kerans 1993; Woodcock et al. 2006). Fracturing, dissolution, collapse, and compaction that created crackle, mosaic, and collapse breccias predated chemical compaction (stylolites). Fracture porosity and inter-clast pores remain open or are filled by anhydrite and salt, rather than by gouge or cataclastic matrix material. Polyphase deformation, slickensides, and shear surfaces associated with fault breccias are not observed. In addition, the absence of polymict clasts or widespread evidence for sieved matrix and clast reworking is inconsistent with fault-derived talus breccias (Mustard and Donaldson 1990).

The unique peloid mudstone–packstone bed in Z-1 is closely associated with underlying brecciated mudstone–wackestones (Fig. 19B), both of which contain fibrous cements lining fractures and pores. Fractures in the peloid mudstone–packstone are circumgranular, producing spherical composite grains instead of angular or fitted breccia clasts of mudstone–wackestone. In muddy, evaporitic, peritidal environments and in experiments, fenestral pores can interlock and produce a diagenetic packstone–grainstone with similar, poorly sorted peloidal grains (Mazzullo and Birdwell 1989). However, the mudstone–wackestone facies underlying the peloid mudstone–packstone is evaporitic but generally not fenestral. Instead, the anastomosing fractures produced a clotted-peloidal fabric more similar to circumgranular glaebules found in Phanerozoic paleocalcretes and modern calcretes (Harrison and Steinen 1978; Wright 1982, 1990, 1994; Armenteros and Daley 1998). Thus, the peloid mudstone–packstone is interpreted as a pedogenic surface developed on top of the lagoonal mudstone–wackestones. While plant roots can play an important role in developing the mechanical texture of such granular pedogenic carbonates and pseudomicrokarsts (Freytet and Verrecchia 2002; Alonso-Zarza and Wright 2010), soil wetting–drying or other abiotic mechanisms may have been sufficient in Ediacaran palustrine environments. Underlying the peloid mudstone–packstone paleosol, the mudstone–wackestones are intensely fractured with solution-enlarged pores. Possibly, below the cored interval of Z-1 Core 1 there was a larger collapsed cave that produced a doline, in which palustrine pedogenesis could have begun in the depression atop the cave-roof mosaic-fracture network.

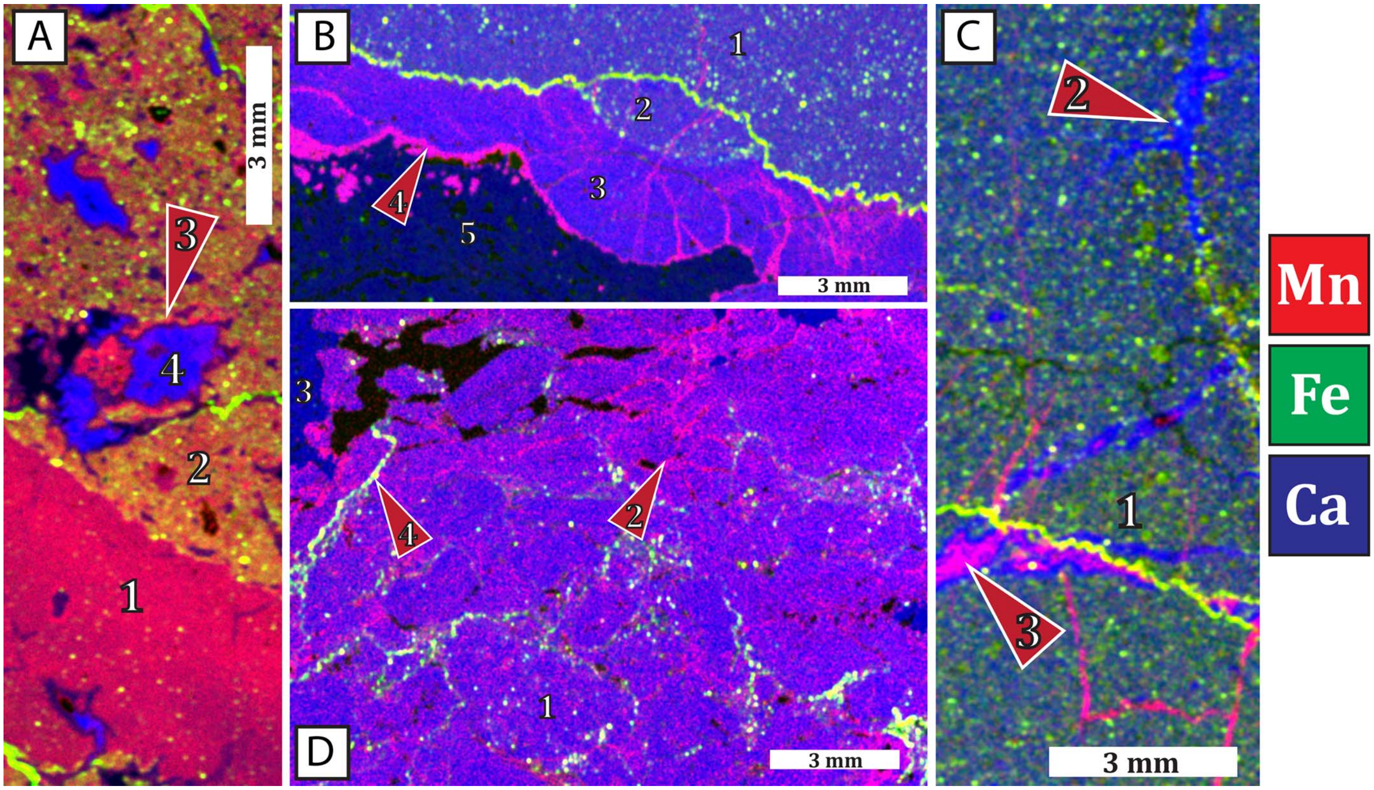

FIG. 17.—Layered Mn (red), Fe (green), and Ca (blue) chemical images to visualize redox-sensitive patterns of diagenesis. Table 1 shows Mn, Fe, and Sr concentrations of annotated carbonate phases. All scale bars are 3 mm. **A)** Thrombolite-intraclast packstone–rudstone with a mudstone intraclast. Mudstone intraclast (1) consists of Mn-rich nonplanar dolomite, while peloid packstone matrix (2) contains much more Fe. Mn-rich fibrous dolomite lines primary pores (3), which were further occluded by zoned (variable Mn-content) poikilitic calcite (4), Y-2 5303.73 m. **B)** Fe-rich dolomitized mudstone (1) with three generations of dolomite cements filling a sheet crack: Fe-rich radiaxial-fibrous dolomite (2), Mn-rich fascicular-optic dolomite (3), and Mn-rich clear bladed dolomite (4). Anhydrite (5) occludes remaining porosity, X-7 3616.64 m. **C)** Fe-rich silty peloid packstone–mudstone (1) with anastomosing fractures interpreted as a palustrine pseudomicrokarst. Anastomosing and circumgranular fractures are lined by Fe-rich fibrous dolomite (2) and filled by clear, Mn-rich, zoned dolomite (3), Z-1 2399.88 m. **D)** Solution-enlarged fracture filled with chaotic clast-supported breccia. Clasts were dolomitized in Mn-rich fluids before brecciation (1), cemented by Mn-rich bladed dolomite (2), and residual pores were filled by anhydrite (3). Fe is concentrated in stylolites at clast boundaries (4), X-7 3623.72 m.

Structural Controls on Development of an Aggradational Platform

The BAC developed as a highly aggradational carbonate platform atop a pre-existing structural high, which it inherited from basin segmentation that began during formation of the Nafun–Ara unconformity. During earliest Ara time, A0C carbonate platforms nucleated unconformably atop Buah carbonate platforms, and, along with basinal siliciclastic strata, mostly flattened remaining pre-Ara topography (Figs. 2A–F, 18A). Deposition of A1C and A2C strata coincided with differential subsidence (Allen 2007; Gómez-Pérez et al. 2024a), permitting aggradation and growth of a steep eastern-escarpment margin. These units along the Birba margin shed limited amounts of carbonate debris into the Athel Trough (Amthor et al. 2005). Both the Birba Platform margin and the Athel Trough subsided more rapidly northward, resulting in thicker and deeper BAC strata nearer Y-2 than Z-1 (Fig. 2G).

In northern Oman, development of a steeper margin also coincided with the tectonic shift from regional subsidence to segmented, faster-subsiding, fault-bounded basins (Amthor et al. 2005; Allen 2007; Cantine et al. 2024; Gómez-Pérez et al. 2024a). In outcrops in the Huqf Mountains, increased tectonic subsidence began with a transition in the lower Buah Formation from a ramp geometry to a distally steepened ramp in the middle and upper Buah Formation, followed by development of the base-Ara unconformity (Cozzi et al. 2004; Nicholas and Gold 2012; Bergmann 2013; Gómez-Pérez et al. 2024a). Like the platforms in the SOSB, these northern Oman carbonate platforms interfinger with silicilytes and siliciclastic basinal strata in pre-existing structural lows (Cozzi et al. 2004; Amthor et al. 2005; Grotzinger and Al-Rawahi 2014; Osburn et al. 2014; Gómez-Pérez et al. 2024a).

Karst Development through Repeated Limited-Duration Exposure

Breccias in the BAC are especially well developed where peritidal dissolution–cementation processes coincided with surficial exposure, meteoric diagenesis, and erosion. Exposure surfaces in the BAC were limited-duration disconformities associated with high-frequency sequence boundaries, and the best-developed karst-collapse breccias and grikes formed at a lower-order (composite) sequence boundary inferred from facies-stacking patterns (Supplemental Information and Fig. 19). The oldest three and one-half carbonate–evaporite sequences (upper A0, A1, A2, and A3) in the Ara Group were deposited in less than 4.1 to 4.7 Myr, yielding an average duration of each sequence of approximately 1.2 to 1.3 Myr (Fig. 1; Bowring et al. 2007), so BAC exposure during higher-order high-frequency and composite sequence boundaries must have occurred over much shorter durations. The period of exposure at high-frequency and composite sequence boundaries was likely shorter than at long-duration megacycle boundaries or lithostratigraphic-formation boundaries from which other large Precambrian paleokarst systems have been recognized (e.g., Kerans 1988; Kerans and Donaldson 1988; Pelechaty et al. 1991; Mathieu et al. 2017).

TABLE 1.—*Concentrations of Mn, Fe, and Sr in carbonate facies and cements shown in Figure 17.*

Sample and Generation	Mn (ppm)	Fe (ppm)	Sr (ppm)
Intraclast rudstone			
(Y-2 5303.73 m, Fig. 17A)			
1 mudstone intraclast	852	346	83
2 peloid packstone matrix	609	2840	78
3 fibrous dolomite	561	280	103
4 poikilitic calcite	411	86	118
Mudstone with sheet crack			
(X-7 3616.64 m, Fig. 17B)			
1 dolomitized mudstone	181	821	76
2 radiaxial-fibrous dolomite	198	552	75
3 fascicular-optic dolomite	239	100	87
4 clear bladed dolomite	638	89	70
Pseudomicrokarst			
(Z-1 2399.88 m, Fig. 17C)			
1 silty peloid packstone–mudstone	167	3745	77
2 fibrous dolomite	157	1737	77
3 clear equant dolomite	485	140	79
Clast-supported breccia			
(X-7 3623.72 m, Fig. 17D)			
1 breccia clast	183	368	75
2 bladed dolomite	885	398	115

Supratidal pisoid rudstones and associated cement boundstones developed meter-scale tepee-shoal complexes, which are typically leached and brecciated during syndepositional intertidal exposure and during later epigenetic diagenesis at sequence boundaries (Assereto and Kendall 1977; Grotzinger 1986; Mutti and Simo 1993). Tepee shoals form supratidal barrier islands (Kendall 1969), which in turn support thin, fresh, groundwater lenses (Budd and Vacher 1991). Dissolution in carbonate-barrier islands happens both at the water table at the tops of these freshwater lenses and at the mixing-zone halocline at the bases of these lenses (Mylroie and Carew 1988, 1990, 1995; Mylroie and Mylroie 2007). The mixing zone is particularly effective because carbonate-mineral undersaturation results from nonlinear changes in carbonate mineral solubility upon mixing of meteoric and marine waters, even when both end-members are individually saturated (Plummer 1975). In evaporitic settings like the BAC shelf crest, dissolution rates in the mixing zone may be enhanced by sulfuric acid, formed from the oxidation of microbially produced sulfide in the halocline (Stoessell et al. 1993; Present et al. 2021). Mn-enriched late cements (Fig. 17; Table 1) may have derived from the suboxic conditions expected near sulfide-oxidation fronts.

In the BAC, fractures in tepee-shoal complexes dominantly produce crackle and mosaic breccias, indicating that wholesale collapse of supratidal facies into paleocave cavities was less common than in-situ compaction. Fractures are almost always solution-enlarged and have salt-rich selvages, and marine cements are heavily leached and recrystallized. These relationships indicate that supratidal environments were exposed long enough to accumulate meteoric diagenetic overprints but not long enough, or were not high enough above sea level, to develop large subsurface cavity networks.

Karst surfaces are not the brecciated-paleocave interval (Lucia 1999). In one case, a sequence boundary and exposure surface in thrombolitic boundstone—recognized by leaching and geopetal silts (Fig. 19A)—is 2 m higher than cave-collapse breccias. Solution-enlarged fractures in supratidal facies may have been points of entry for meteoric water through permeable tepee-pisolite facies. These fractures are associated with mosaic breccias and small chaotic breccias. Grikes filled with clast-supported breccias also are found predominantly in shelf-crest and lagoonal facies (Fig. 19C). Other less permeable facies may have been stronger cave ceilings that were horizontally or vertically removed from infiltration areas and were more associated with crackle and mosaic breccias.

The thickness of brecciated intervals that represent collapsed caverns can constrain the original pore volume. Collapse compacts open void space into breccia with lower porosity; thus, breccia thickness is greater than the original cave height (Loucks 1999). Brecciated intervals in X-7 have total porosities of 10–15%, representing the post-collapse porosity of caves that had primary porosities close to 100%. Therefore, 2–5-m-thick breccia intervals represent original pores 61 cm to 1.9 m tall; this is an upper estimate if post-collapse dissolution increased the porosity of the collapse breccia. The maximum pore sizes are similar in size to those produced by thin freshwater lenses in low-relief supratidal carbonate islands, and the largest were tall enough to have formed by vertical vadose water flow responsible for producing grikes and flowstones (Craig 1988; Budd and Vacher 1991; Tinker et al. 1995).

Multiple phases of phreatic and vadose diagenesis overprint the collapse breccias and grike fills. Angular breccia clasts are cemented by bladed dolomite, have palimpsest columnar cements, and have grumelous overgrowths and geopetal micrite interpreted as phreatic diagenetic features, which were then further leached, producing moldic pores and fabric-destructive recrystallized fabrics in a vadose environment (Fig. 15J–L). Thus, exposure, dissolution, and collapse in a vadose meteoric environment predated re-inundation and later phreatic diagenesis, before at least one additional instance of vadose diagenesis before burial. Chemical images indicate that, while breccia clasts and micrite envelopes are in some cases enriched in Fe and formed in anoxic environments, the latest cement textures formed from suboxic fluids with Mn (Fig. 17; Table 1). Together, these observations suggest that karst surfaces and related breccias remained close to sea level, permitting repeated reinundation with later relative-sea-level cycles.

Pendant cements and cavity-filling isopachous cements, which are clearly associated with sheet cracks in supratidal facies, might closely resemble karst-related vug and cave-filling cements such as speleothems or flowstones (Assereto and Folk 1980). Flowstones that form in a near-surface peritidal environment share many features with those formed in telegenetic karst caverns, including heteromineralogic isopachous and fibrous cements, polyphase precipitation, intergrowth with iron-rich internal carbonate sediments (*terra rossa*), and cementation of collapsed host-rock clasts and nodular to pisoidal authigenic grains (Folk and Assereto 1976; Assereto and Folk 1980; Chafetz and Butler 1980; Bar-Matthews et al. 1991; Ding et al. 2019). The cements associated with both collapse breccias and supratidal tepee-shoal breccias in the BAC are similarly interpreted as flowstones. Isopachous and festoon cements in supratidal tepee-pisolite facies reach 40 cm thick and formed before compactional mosaic brecciation, indicating that pores with dimensions comparable to those calculated from breccia collapse once existed. The development of breccias and flowstones from polyphase dissolution and compaction implies smaller original pores than the upper estimates from the thicknesses of collapse breccias, further consistent with repeated, modest exposure intervals. The flowstones were almost surely epigenetic and latest Ediacaran age, because any uplift and exposure throughout the Phanerozoic would have removed the overlying Ara evaporites. That said, as for breccias (Table 2), differentiating purely syndepositional-cement boundstones formed in evaporitic supratidal environments from flowstones formed in epigenetic karsts is challenging. Many of the features that might distinguish precipitates formed in depositional environments from those formed in the shallow subsurface are obscured by the pervasive recrystallization and dolomitization of the BAC. Such features may be more readily preserved in silicified paleokarsts (e.g., Mustard and Donaldson 1990; Skotnicki and Knauth 2007; Ding et al. 2019; Moore et al. 2024).

In post-Silurian settings, carbonate-dissolution rates in shallow vadose zones and soils are enhanced by soil pCO_2 that exceeds atmospheric concentrations by one to two orders of magnitude because of plant-root

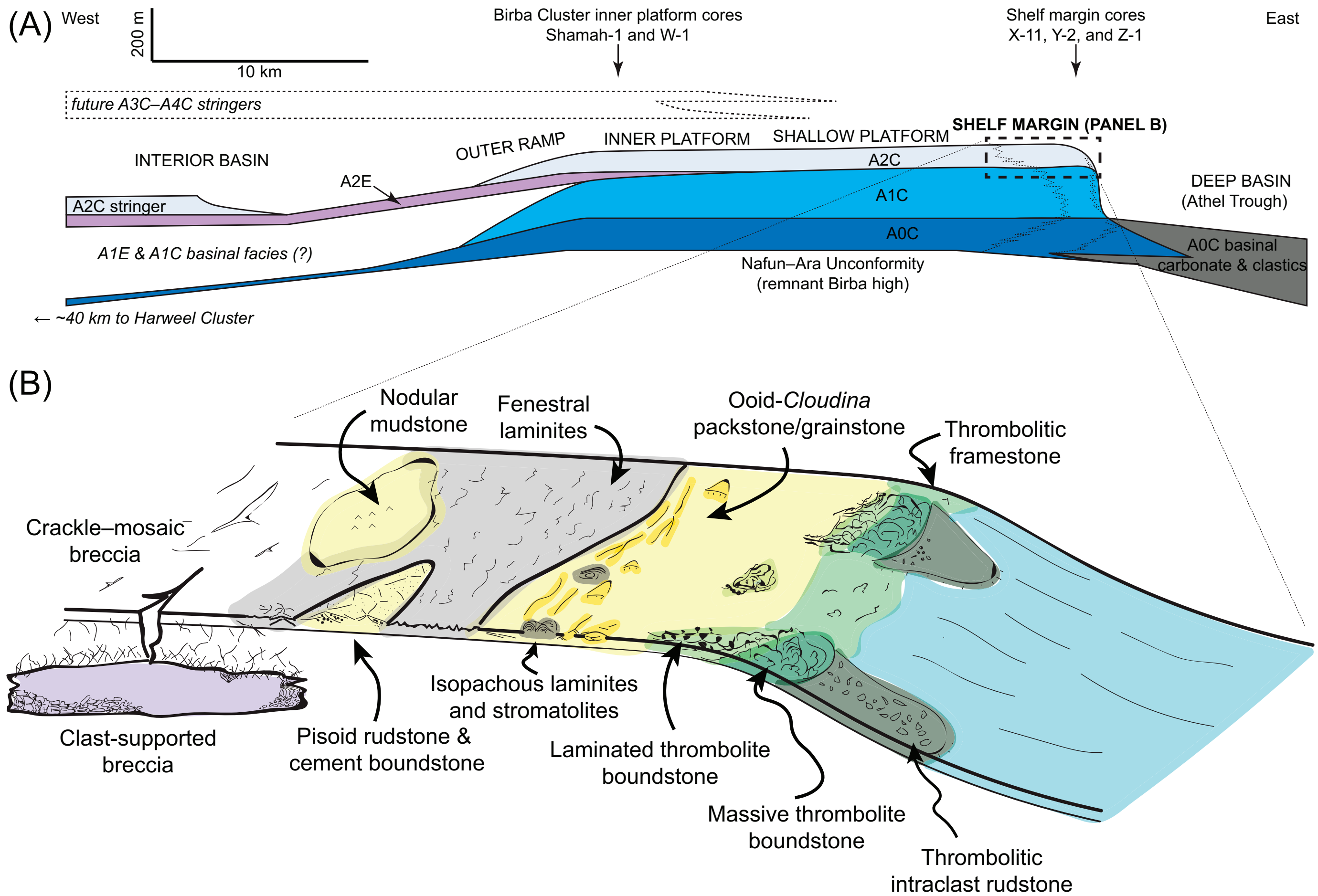

FIG. 18.—**A)** Birba Platform depositional model at the end of A2C deposition (compare geometries to Fig. 2B or D, and environment map in Fig. 2H). Rectangle situates the facies model developed here for the shelf-margin environment, which is situated on the eastern side of a structural high between the Athel Trough and a platform interior basin separating the Birba Cluster from the Harweel Cluster. **B)** Interpreted depositional environments for lithofacies described in BAC shelf-margin cores.

respiration and organic-matter decomposition (Brasier 2011; Gulley et al. 2014). Although subterranean microbial activity can drive organic-matter oxidation (Gulley et al. 2014), this mechanism is typically not thought to have been important during Ediacaran time, which predates the evolution of vascular land plants. However, alternative dissolution mechanisms may have produced karst features in pre-vegetation settings. First, elevated Proterozoic atmospheric pCO_2 would have increased the carbonic acid content of meteoric waters directly equilibrated with the atmosphere, although latest Ediacaran pCO_2 is poorly constrained (Holland and Zbinden 1988; Krissansen-Totton et al. 2018; Strauss and Tosca 2020). Second, mixing-zone dissolution at the halocline beneath freshwater lenses can drive carbonate dissolution even when both meteoric and marine end-member fluids are saturated with respect to carbonate minerals (Plummer 1975; Mylroie and Carew 1990). Both carbonate dissolution and precipitation might have been augmented by seasonal, tidal, and/or diurnal temperature and salinity changes in either endmember (Dreybrodt 1982; Gulley et al. 2014). Third, microbial sulfate reduction at the halocline produces sulfide, which upon oxidation generates sulfuric acid that enhances dissolution (Stoessell et al. 1993; Mylroie and Mylroie 2007). Together, these processes can produce the karst features observed in the BAC during relatively short exposure periods. Elevated atmospheric pCO_2, mixing-zone dissolution, and respiration-driven porewater acidification also promote early dolomitization (Rivers 2023), consistent with the close paragenetic relationship between dissolution and pervasive early dolomitization in the BAC.

Development of a Hydrographic Barrier in a Shelf-Crest Facies Tract

Early work on Ara Group stratigraphy suggests that the shelf-margin thrombolite reefs comprised the shallowest, geomorphically highest point along the shelf margin, and thus were the cause of hydrographic restriction westward towards the platform interior (Mattes and Conway Morris 1990). However, their mud-rich nature, lack of bedforms, and interfingering with shallower grainy facies indicate that they formed in a deeper, subtidal setting. Other thrombolite or calcimicrobial bioherms have been identified in subtidal settings in Proterozoic carbonate systems, both elsewhere in the Ara Group (Al-Siyabi 2005; Schröder et al. 2005; Grotzinger and Al-Rawahi 2014) and globally (Sami and James 1994; Adams et al. 2004; Batten et al. 2004; DiBenedetto and Grotzinger 2005; Wallace et al. 2015). Similar shelf-margin or upper-slope boundstones have also been recognized recently in Phanerozoic strata (Della Porta et al. 2003; Kenter et al. 2005; Collins et al. 2013; Playton and Kerans 2018; Kelley et al. 2020, 2024). In all of these settings, grainstones and peritidal microbial facies occupy shallower open-shelf or platform-interior settings than the subtidal thrombolite reefs forming at the shelf margin or the break in slope on the rim.

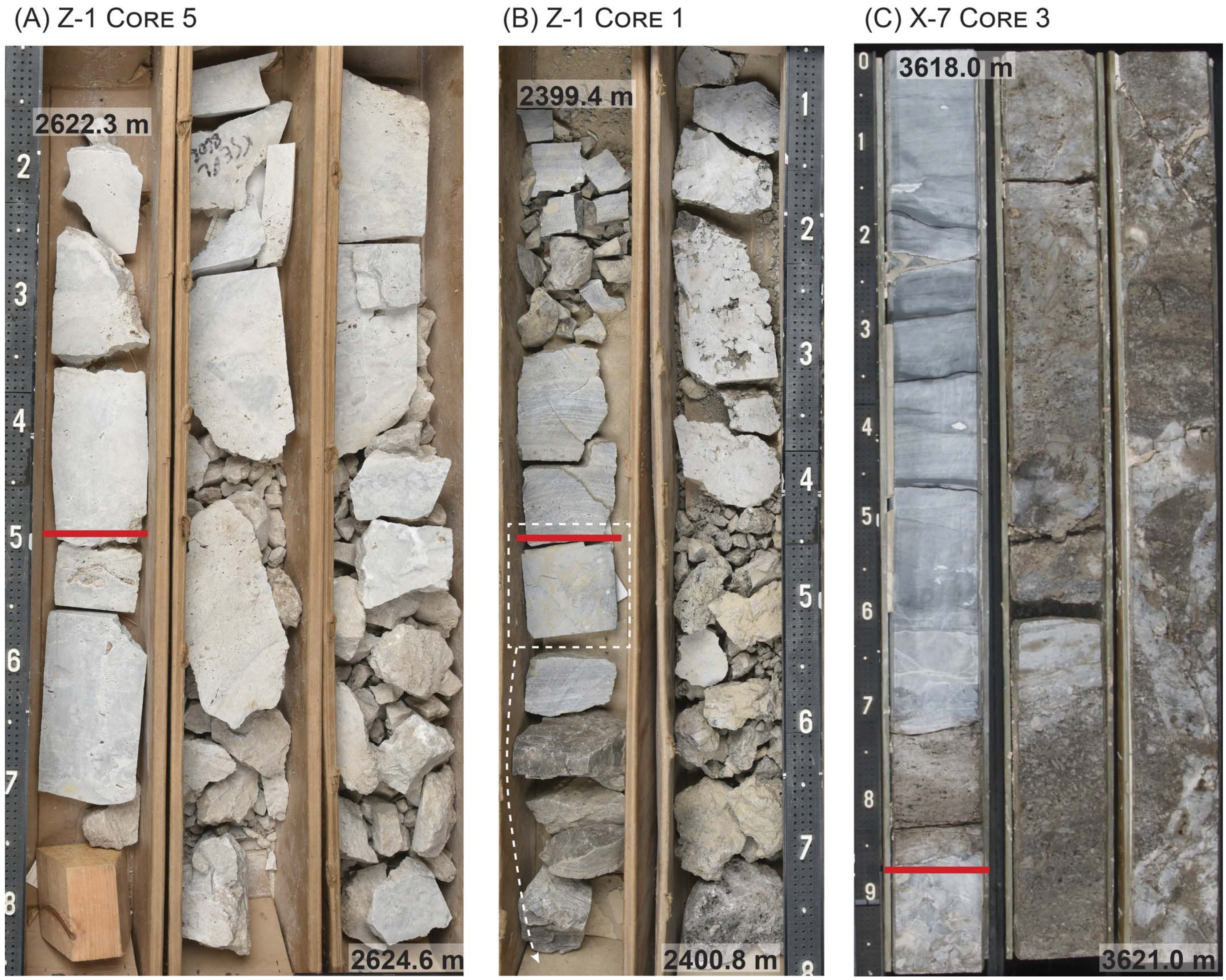

FIG. 19.—Core-box photographs of examples of sequence boundaries showing different styles of exposure surfaces in the BAC. Scale is in decimeters. **A)** Leached surface with solution-enlarged pores containing geopetal silt in thrombolitic boundstone, Z-1 Core 5 at 2622.8 m. The surface is about 2 m above an anhydrite-cemented clast-supported breccia with geopetal cements and internal sediment at 2624.3 m. **B)** Pseudomicrokarst overlying rubbly, leached lagoonal mudstones and abruptly overlain by subtidal isopachous laminites, Z-1 Core 1 at 2399.9 m. Dashed arrow indicates that the core segment with pseudomicrokarst belongs at the base of the core box, where it was located in original core photographs from 1977. **C)** Stylolitic surface in evaporitic lagoonal facies overlying several meters of leached clast-supported breccias and grikes, X-7 Core 3 at 3618.9 m. This surface is interpreted as the A1–A2 composite sequence boundary (see Supplemental Information), with the overlying greenish dolomitic siltstone interpreted as volcanic ash reworked in a subtidal lagoon.

Interpretation of the thrombolite reefs as deeper shelf-margin deposits at the shelf–slope break places the main hydrographic barrier inboard of the grainy outer shelf, in a shelf crest composed of supratidal tepee-pisolite and fenestral-laminite facies. This barrier separated subtidal outer-shelf facies on the eastern escarpment margin from evaporitic, subtidal back-barrier lagoonal facies on the western platform interior. The development of a hydrographic barrier was a consequence of the stable, aggradational platform architecture. A higher rate of aggradation relative to progradation produces higher positive elevation of tepee-shoal complexes during highstands (Grotzinger 1986; Kerans and Tinker 1999; Rush and Kerans 2010). This higher relief and more stable shoreline permit more vadose diagenetic alteration and/or erosion at lowstands (manifested as karst breccias described above), as well as marine cementation and lithification at highstands (Grotzinger 1986; Kerans and Tinker 1999).

Two complementary mechanisms may contribute to a preservation bias for shoal-grainstone facies at the expense of up-dip microbial-laminite facies. First, because lithification of microbial communities requires the appropriate balance between community respiration and productivity, benthic microbial communities may have been more widespread throughout the grainy shelf facies than where they are preserved, with their presence belied only by occasional crinkly laminations and intraclasts (Present et al. 2021). An excess of benthic and shallow phreatic microbial respiration favors dissolution of primary carbonate minerals and inhibits their preservation (Walter and Burton 1990; Walter et al. 1993; Reid et al. 2000; Present et al. 2021), although it may favor early replacement dolomitization akin to what is seen throughout the Birba Formation (Rivers et al. 2021; Rivers 2023).

Second, grainy carbonate shoals often aggrade into migrating-barrier sandbar complexes, which sometimes prograde basinward by shoreface

TABLE 2.—*Criteria for distinguishing depositional and diagenetic breccia fabrics, which may be gradational in peritidal facies.*

Syndepositional → Early marine–vadose diagenesis → Postdepositional collapse breccias			
Reef-Derived Packstone–Rudstones	Supratidal Rudstones and Tepee-Pisolites	Crackle and Mosaic Breccias	Collapse Breccias
• Partially lithified intraclasts • Marine allochems in wackestone–packstone matrix • Marine cements and absence of vadose cements • Sedimentary structures consistent with depositional environment	• Brecciated peritidal facies • Shrinkage cracks and/or sheet cracks • Multiple generations of cementation and fracturing • Erosional and/or exposure surfaces	• *In situ* brecciation and fitted fabric • Relationship with solution-enlarged fracture and/or vug porosity	• Massive and poorly sorted • Anhydrite- and salt-cemented clasts • Laminated cave-floor grainstones • Meteoric diagenetic textures, including moldic pores and vadose cements • Brecciation before and synchronous with compaction • Association with crackle and mosaic breccias

accretion but more often retrograde over intertidal and subtidal lagoonal complexes during transgressions (Dalrymple and Rivers 2023; Rivers and Dalrymple 2025). This retrogradation occurs with shoreface erosion at the basinward side of the sandbars, resulting in reworking or erosion of up-dip facies. Thus, fenestral-laminite and stromatolite facies behind these sandbars may have formed in semi-open pro-barrier lagoons and were either covered by open-platform sands, tidal-inlet grainstone complexes, or reworked during transgressions. Such stromatolite lagoons would have been in front of the tepee-pisolite barrier complex developed up-dip among fenestral laminites. Early lithification of the microbial laminites would have preserved them, but the combined effects of microbial processes that inhibit lithification and the reworking by mobile-sand shoals might have obscured their original extent.

These effects on the preservation of microbial-laminite facies may have been counteracted, in part, by the intense early lithification of the up-dip tepee-pisolite barrier complex. Lagoonward expansion of the barrier towards the platform interior is recognized by vertical stacking patterns of lagoonal facies overlain by increasingly thin supratidal barrier facies (e.g., sequence from 3618 to 3602 m in well X-7, Fig. 3B, Supporting Information). Supratidal tepee complexes form barriers from high-alkalinity groundwater derived from marine phreatic fluids, and pisoids reflect high carbonate mineral saturation states in surface waters (Smith et al. 2021). Together, the intense cementation of tepees and syndepositional lithification of pisolitic grains likely inhibited backstepping and transgression on the eastern, energetic, basinward side of the barrier complex. This is manifested as brecciation and leaching of pisoids and tepee-cement boundstones. The syndepositional lithification and intense cementation that characterized the tepee-pisolite barrier complex contrasts with mobile carbonate-sand barriers in modern systems, where more limited early cementation does not prevent landward migration during transgression (Rivers et al. 2020). Thus, the barrier complex broadened platformward, rather than transgressed away from the Athel Trough in a pattern that is similar to barrier widening by lagoonward progradation on rimmed shelves in other Proterozoic platforms (Grotzinger 1986; Sami and James 1994).

Aggradational stacking of tepee barrier shoals, resulting in nearly continuous development of many limited-duration disconformities, may explain why karst was less well developed in more progradational peritidal carbonate sequences in the Huqf Supergroup, such as the Khufai and Buah formations and the A0C sequence of the BAC. The tepee complexes and associated synsedimentary breccias in Nafun Group carbonate ramps formed in a regime of slower tectonic subsidence (Cozzi et al. 2004; Bergmann 2013; Osburn et al. 2014; Gómez-Pérez et al. 2024a). In the lowest parts of the BAC, A0C carbonate units also show a broad, ramp-like seismic geometry that thickens northward and eastward as it interfingers with A0 siliciclastic strata (Fig. 2). As cored in Z-1, these strata are interpreted as low-energy mid-platform facies consisting of mottled, peloidal packstones to grainstones with sheet cracks and seafloor cements interpreted to have formed in shelf-top subtidal environments (Fig. 9C), but no breccias or well-developed karst (Supplemental Information). Well cuttings and gamma-ray logs indicate that these grainy carbonates interfinger with siliciclastic or volcaniclastic-rich strata that onlap the unconformity at the top of the Nafun Group (Fig. 2), and may be similar to ash-rich and clastic-rich basinal carbonate facies in the deepest parts of the Athel Trough east of the Birba Platform margin (Bowring et al. 2007; Forbes et al. 2010; Gómez-Pérez et al. 2024a). Thus, the broader, more progradational deposition of Buah and lowermost BAC strata may predate the development of a well-defined hydrographic barrier and a steep eastern escarpment margin associated with the more aggradational A1 and A2 sequences.

Although limited platform exposure, despite apparently shallow peritidal depositional environments, is a hallmark of Ara Group deposition, locations with aggradational strata atop stable platform geometries accumulate karstic breccias. In well-developed Ara stringers, anhydrite that formed in supratidal salinas during late highstands is conformably overlain by lowstand-systems-tract halite (Schröder et al. 2003; Grotzinger and Al-Rawahi 2014). In general, salt deposition may have limited the positive relief of stringer carbonate platforms, resulting in more progradational geometries than A1C and younger strata along the eastern BAC margin (Schröder et al. 2003; Grotzinger and Al-Rawahi 2014). A notable exception is the A2-age stringer platform in the Harweel Cluster (Fig. 1A), which is unusual among stringers in having a steep platform margin (Grotzinger and Al-Rawahi 2014), a feature it shares with BAC strata. For example, in well Sakhiya-4, the A2C contains a collapse breccia in aggradational strata assigned to a transgressive systems tract that is abruptly overlain by an unconformity without progradational highstand-systems-tract strata (Grotzinger and Al-Rawahi 2014).

The sequence boundaries identified from facies stacking patterns and accumulated exposure thus provide stratigraphic markers for the aggradational Birba Platform, where the lower carbonate cycles lack the thick evaporite intervals that define cycle boundaries in coeval stringers and younger Ara strata. Correlation across the segmented SOSB and to coeval strata in the Huqf Mountains, north Oman, and other eastern Gondwanan basins remains challenging because of differential subsidence and facies heterogeneity (Gómez-Pérez et al. 2024a). The recognition of sequence boundaries and karst features along the BAC margin provides a foundation for such correlation in subsurface and outcropping strata.

CONCLUSIONS

The BAC is a critical stratigraphic interval in the SOSB, formed just before the Ediacaran–Cambrian boundary at a key tectonic transition during the latest assembly of Gondwana. The BAC shelf margin developed as an asymmetric barrier complex comprising a shelf-crest shoal complex that separated outer-shelf grainstones and shelf-margin reefs from highly restricted inner-shelf lagoonal carbonates and evaporites. This barrier system developed following a regional shift from thermal subsidence (Nafun Group) to rapid differential subsidence linked to eastward migration of the Western Deformation Front. Critically, the persistence of structural highs beneath the Birba Platform enabled highly aggradational carbonate growth that maintained pace with subsidence, creating the repeated exposure, brecciation, and cementation of peritidal facies necessary for a stable shelf-crest barrier complex to form.

Occasional exposure of the shelf crest during sea-level lowstands produced distinctive karst breccias that combine syndepositional supratidal brecciation with epigenetic karst overprinting. These features have polyphase dissolution and precipitation textures formed before stylolite development, with chemical imaging revealing Mn enrichment indicative of near-surface suboxic conditions during the latest stages of fabric development. The pervasive nature of karsting over several meters of strata, including collapsed pores below exposure surfaces, necessitates the use of facies stacking patterns rather than individual exposure surfaces to identify sequence boundaries. This approach to sequence-boundary identification may be particularly critical in Precambrian carbonates, which lack diagnostic terrestrial biotic features that facilitate karst and exposure recognition in Phanerozoic strata. Furthermore, although syndepositional and epigenetic breccias in the BAC are genetically related and have gradational fabrics, systematic analysis of cement generations and dissolution textures enables their differentiation.

Exposure surfaces and karst-related brecciation of the Birba Formation contrast markedly with younger Ara stringers, which typically show abrupt transitions to sulfates without platform exposure. This distinction reflects the unique tectonic configuration during Ara deposition, when structural lows were partially filled while adjacent structural highs supported aggradational carbonate platforms capable of maintaining emergent conditions. The transpressive tectonic evolution thus fundamentally controlled both the architecture of the basal Ara carbonates and the development of cyclic carbonate–evaporite deposition that characterizes the Ara Group stratigraphy.

ACKNOWLEDGMENTS

This research was funded by Petroleum Development Oman (PDO). TMP was additionally supported by Simons Foundation Grant 668346. The PDO Sedimentology group and the PDO core-shed staff are greatly thanked for their help. We also thank Anne Fetrow, Charlie Kerans, John Rivers, Bob Dalrymple, Dave Eby, and Maggie Osburn, who provided thoughtful and helpful discussion. Reviews by Alex Brasier and an anonymous reviewer, and insightful editing by John Southard, greatly improved this manuscript.

REFERENCES

Adams, E.W., Schröder, S., Grotzinger, J.P., and McCormick, D.S., 2004, Digital reconstruction and stratigraphic evolution of a microbial-dominated, isolated carbonate platform (terminal Proterozoic, Nama Group, Namibia): Journal of Sedimentary Research, v. 74, p. 479–497, doi:10.1306/122903740479.

Allen, P.A., 2007, The Huqf Supergroup of Oman: basin development and context for Neoproterozoic glaciation: Earth-Science Reviews, v. 84, p. 139–185, doi:10.1016/j.earscirev.2007.06.005.

Al-Marjeby, A., and Nash, D., 1986, A summary of the geology and oil habitat of the Eastern Flank Hydrocarbon Province of South Oman: Marine and Petroleum Geology, v. 3, p. 306–314, doi:10.1016/0264-8172(86)90035-8.

Alonso-Zarza, A.M., and Wright, V.P., 2010, Palustrine Carbonates, *in* Alonso-Zarza, A.M., and Tanner, L.H., eds., Carbonates in continental settings: facies, environments, and processes: Amsterdam, Elsevier, Developments in Sedimentology 61, p. 103–131, doi:10.1016/S0070-4571(09)06102-0.

Al-Siyabi, H.A., 2005, Exploration history of the Ara intrasalt carbonate stringers in the South Oman Salt Basin: GeoArabia, v. 10, p. 39–72.

Amthor, J.E., Grotzinger, J.P., Schröder, S., Bowring, S.A., Ramezani, J., Martin, M.W., and Matter, A., 2003, Extinction of *Cloudina* and *Namacalathus* at the Precambrian–Cambrian boundary in Oman: Geology, v. 31, p. 431–434, doi:10.1130/0091-7613(2003)031<0431:EOCANA>2.0.CO;2.

Amthor, J.E., Ramseyer, K., Faulkner, T., and Lucas, P., 2005, Stratigraphy and sedimentology of a chert reservoir at the Precambrian–Cambrian boundary: the Al Shomou Silicilyte, South Oman Salt Basin: GeoArabia, v. 10, p. 89–122.

Amthor, J.E., Ramseyer, K., Matter, A., Pettke, T., and Fallick, A.E., 2015, Diagenesis of a light, tight-oil chert reservoir at the Ediacaran–Cambrian boundary, Sultanate of Oman: GeoArabia, v. 20, p. 147–178.

Armenteros, I., and Daley, B., 1998, Pedogenic modification and structure evolution in palustrine facies as exemplified by the Bembridge Limestone (Late Eocene) of the Isle of Wight, southern England: Sedimentary Geology, v. 119, p. 275–295, doi:10.1016/S0037-0738(98)00067-0.

Assereto, R., and Folk, R.L., 1980, Diagenetic fabrics of aragonite, calcite, and dolomite in an ancient peritidal-spelean environment: Triassic Calcare Rosso, Lombardia, Italy: Journal of Sedimentary Petrology, v. 50, p. 371–394, doi:10.1306/212F7A0E-2B24-11D7-8648000102C1865D.

Assereto, R.L., and Kendall, C.G., 1977, Nature, origin and classification of peritidal tepee structures and related breccias: Sedimentology, v. 24, p. 153–210, doi:10.1111/j.1365-3091.1977.tb00254.x.

Bar-Matthews, M., Matthews, A., and Ayalon, A., 1991, Environmental controls of speleothem mineralogy in a karstic dolomitic terrain (Soreq Cave, Israel): The Journal of Geology, v. 99, p. 189–207.

Barnaby, R.J., and Rimstidt, J.D., 1989, Redox conditions of calcite cementation interpreted from Mn and Fe contents of authigenic calcites: Geological Society of America, Bulletin, v. 101, p. 795–804, doi:10.1130/0016-7606(1989)101<0795:RCOCCI>2.3.CO;2.

Barnaby, R.J., and Ward, W.B., 2007, Outcrop analog for mixed siliciclastic–carbonate ramp reservoirs: stratigraphic hierarchy, facies architecture, and geologic heterogeneity: Grayburg Formation, Permian Basin, U.S.A.: Journal of Sedimentary Research, v. 77, p. 34–58, doi:10.2110/jsr.2007.007.

Batten, K.L., Narbonne, G.M., and James, N.P., 2004, Paleoenvironments and growth of early Neoproterozoic calcimicrobial reefs: platformal Little Dal Group, northwestern Canada: Precambrian Research, v. 133, p. 249–269, doi:10.1016/j.precamres.2004.05.003.

Beeunas, M.A., and Knauth, L.P., 1985, Preserved stable isotopic signature of subaerial diagenesis in the 1.2-b.y. Mescal Limestone, central Arizona: implications for the timing and development of a terrestrial plant cover: Geological Society of America, Bulletin, v. 96, p. 737–745, doi:10.1130/0016-7606(1985)96<737:PSISOS>2.0.CO;2.

Bergmann, K.D., 2013, Constraints on the carbon cycle and climate during the early evolution of animals [Ph.D. Thesis]: California Institute of Technology, Pasadena, California, 417 p., http://resolver.caltech.edu/CaltechTHESIS:06102013-045943358.

Bergmann, K.D., Osburn, M.R., Anderson, N.T., Hayhow, C., Wilcots, J., Cantine, M.D., Fischer, W.W., and Bonifacie, M., 2025, Origins and alteration of Ediacaran carbonates recording the Shuram Excursion in Oman: Geochemistry, Geophysics, Geosystems, v. 26, doi:10.1029/2025GC012161.

Bowring, S.A., Grotzinger, J.P., Condon, D.J., Ramezani, J., Newall, M.J., and Allen, P.A., 2007, Geochronologic constraints on the chronostratigraphic framework of the Neoproterozoic Huqf Supergroup, Sultanate of Oman: American Journal of Science, v. 307, p. 1097–1145.

Brasier, A.T., 2011, Searching for travertines, calcretes and speleothems in deep time: processes, appearances, predictions and the impact of plants: Earth-Science Reviews, v. 104, p. 213–239, doi:10.1016/j.earscirev.2010.10.007.

Budd, D.A., and Vacher, H.L., 1991, Predicting the thickness of fresh-water lenses in carbonate paleo-islands: Journal of Sedimentary Petrology, v. 61, p. 43–53, doi:10.1306/D4267681-2B26-11D7-8648000102C1865D.

Butterfield, N.J., and Grotzinger, J.P., 2012, Palynology of the Huqf Supergroup, Oman: Geological Society of London, Special Publications, v. 366, p. 251–263, doi:10.1144/SP366.10.

Cantine, M.D., Knoll, A.H., and Bergmann, K.D., 2020, Carbonates before skeletons: a database approach: Earth-Science Reviews, v. 201, doi:10.1016/j.earscirev.2019.103065.

Cantine, M.D., Rooney, A.D., Knoll, A.H., Gómez-Pérez, I., al Baloushi, B., and Bergmann, K.D., 2024, Chronology of Ediacaran sedimentary and biogeochemical shifts along eastern Gondwanan margins: Communications Earth & Environment, v. 5, p. 1–9, doi:10.1038/s43247-024-01630-1.

Chafetz, H.S., and Butler, J.C., 1980, Petrology of recent caliche pisolites, spherulites, and speleothem deposits from central Texas: Sedimentology, v. 27, p. 497–518, doi:10.1111/j.1365-3091.1980.tb01644.x.

Chen, Z., Bengtson, S., Zhou, C.M., Hua, H., and Yue, Z., 2008, Tube structure and original composition of *Sinotubulites*: shelly fossils from the late Neoproterozoic in southern Shaanxi, China: Lethaia, v. 41, p. 37–45, doi:10.1111/j.1502-3931.2007.00040.x.

Clarke, M.W.H., 1988, Stratigraphy and rock unit nomenclature in the oil-producing area of interior Oman: Journal of Petroleum Geology, v. 11, p. 5–60, doi:10.1111/j.1747-5457.1988.tb00800.x.

Collins, J., Narr, W., Harris, P.M., Playton, T., Jenkins, S., Tankersley, T., and Kenter, J.A.M., 2013, Lithofacies, depositional environments, burial diagenesis, and dynamic field behavior in a Carboniferous slope reservoir, Tengiz Field (Republic of Kazakhstan), and comparison with outcrop analogs, *in* Verwer, K., Playton, T.E., and Harris, P.M., eds., Deposits, Architecture, and Controls of Carbonate Margin, Slope and Basinal Settings: SEPM, Special Publication 105, p. 50–83, doi:10.2110/sepmsp.105.11.

Conway Morris, S., Mattes, B.W., and Menge, C., 1990, The early skeletal organism Cloudina: new occurrences from Oman and possibly China: American Journal of Science, v. 290-A, p. 245–260.

Cozzi, A., Grotzinger, J.P., and Allen, P.A., 2004, Evolution of a terminal Neoproterozoic carbonate ramp system (Buah Formation, Sultanate of Oman): effects of basement paleotopography: Geological Society of America, Bulletin, v. 116, p. 1367–1384, doi:10.1130/B25387.1.

Craig, D.H., 1988, Caves and other features of Permian karst in San Andres Dolomite, Yates Field Reservoir, West Texas, *in* James, N.P., and Choquette, P.W., eds., Paleokarst: New York, Springer-Verlag, p. 342–363, doi:10.1007/978-1-4612-3748-8_17.

Cross, N.E., van Veen, L.-J., Al-Enezi, A., Singh, S., and van Beusekom, G., 2021, Seismic geomorphology of karst in Cretaceous to early Cenozoic carbonates of North Kuwait: Marine and Petroleum Geology, v. 128, doi:10.1016/j.marpetgeo.2021.104947.

Cruz, F.E.G., and Eberli, G.P., 2019, Co-existence of skeletal and ooid shoals as a result of antecedent topography: Cat Cay shoal complex, Bahamas: The Depositional Record, v. 5, p. 451–468, doi:10.1002/dep2.90.

Dalrymple, R.W., and Rivers, J.M., 2023, A new look at modern carbonate shoals and coastal barrier systems: Earth-Science Reviews, v. 246, doi:10.1016/j.earscirev.2023.104553.

De Wit, M.J., Linol, B., and Nengovhela, V., 2020, Proterozoic–Paleozoic sedimentary rocks and Mesozoic–Cenozoic landscapes of the Cape Mountains across the Kango Complex reveal "More Gaps Than Record" from Rodinia and Gondwana to Africa: Geoscience Canada, v. 47, p. 7–58, doi:10.12789/geocanj.2020.47.157.

Della Porta, G., Kenter, J.A.M., Bahamonde, J.R., Immenhauser, A., and Villa, E., 2003, Microbial boundstone dominated carbonate slope (Upper Carboniferous, N Spain): microfacies, lithofacies distribution and stratal geometry: Facies, v. 49, p. 175–207, doi:10.1007/s10347-003-0031-0.

DiBenedetto, S., and Grotzinger, J.P., 2005, Geomorphic evolution of a storm-dominated carbonate ramp (c. 549 Ma), Nama Group, Namibia: Geological Magazine, v. 142, p. 583–604, doi:10.1017/S0016756805000890.

Dill, R.F., Shinn, E.A., Jones, A.T., Kelly, K., and Steinen, R.P., 1986, Giant subtidal stromatolites forming in normal salinity waters: Nature, v. 324, p. 55–58, doi:10.1038/324055a0.

Ding, Y., Chen, D., Zhou, X., Guo, C., Huang, T., and Zhang, G., 2019, Cavity-filling dolomite speleothems and submarine cements in the Ediacaran Dengying microbialites, South China: responses to high-frequency sea-level fluctuations in an "aragonite–dolomite sea": Sedimentology, v. 66, p. 2511–2537, doi:10.1111/sed.12605.

Dravis, J.J., 1983, Hardened subtidal stromatolites, Bahamas: Science, v. 219, p. 385–386, doi:10.1126/science.219.4583.385.

Dreybrodt, W., 1982, A possible mechanism for growth of calcite speleothems without participation of biogenic carbon dioxide: Earth and Planetary Science Letters, v. 58, p. 293–299, doi:10.1016/0012-821X(82)90202-3.

Esteban, M., and Klappa, C.F., 1983, Subaerial exposure environment, *in* Scholle, P.A., Bebout, D.G., and Moore, C.H., eds., Carbonate Depositional Environments: American Association of Petroleum Geologists, Memoir 33, p. 1–54, doi:10.1306/M33429C1.

Fike, D.A., and Grotzinger, J.P., 2008, A paired sulfate–pyrite $\delta^{34}S$ approach to understanding the evolution of the Ediacaran–Cambrian sulfur cycle: Geochimica et Cosmochimica Acta, v. 72, p. 2636–2648, doi:10.1016/j.gca.2008.03.021.

Fischer, A.G., 1964, The Lofer Cyclothems of the Alpine Triassic, *in* Merriam, D.F., ed., Symposium on Cyclic Sedimentation: State Geological Survey of Kansas, Bulletin 169, p. 107–149, https://www.kgs.ku.edu/Publications/Bulletins/169/Fischer/index.html.

Folk, R.L., and Assereto, R., 1976, Comparative fabrics of length-slow and length-fast calcite and calcitized aragonite in a Holocene speleothem, Carlsbad Caverns, New Mexico: Journal of Sedimentary Petrology, v. 46, p. 486–496, doi:10.1306/212F6FCD-2B24-11D7-8648000102C1865D.

Forbes, G.A., Jansen, H.S., and Schreurs, J., 2010, Lexicon of Oman Subsurface Stratigraphy: Reference Guide to the Stratigraphy of Oman's Hydrocarbon Basins: Manama, Bahrain, Gulf PetroLink, 373 p.

Fralick, P., and Riding, R., 2015, Steep Rock Lake: sedimentology and geochemistry of an Archean carbonate platform: Earth-Science Reviews, v. 151, p. 132–175, doi:10.1016/j.earscirev.2015.10.006.

Freytet, P., and Verrecchia, E.P., 2002, Lacustrine and palustrine carbonate petrography: an overview: Journal of Paleolimnology, v. 27, p. 221–237, doi:10.1023/A:1014263722766.

Friedman, G.M., 1959, Identification of carbonate minerals by staining methods: Journal of Sedimentary Petrology, v. 29, p. 87–97, doi:10.1306/74d70894-2b21-11d7-8648000102c1865d.

Goldhammer, R.K., Dunn, P.A., and Hardie, L.A., 1990, Depositional cycles, composite sea-level changes, cycle stacking patterns, and the hierarchy of stratigraphic forcing: examples from Alpine Triassic platform carbonates: Geological Society of America, Bulletin, v. 102, p. 535–562, doi:10.1130/0016-7606(1990)102<0535:DCCSLC>2.3.CO;2.

Gómez-Pérez, I., and Morton, A., 2025, Neoproterozoic–early Paleozoic tectonic evolution of Oman revisited: implications for the consolidation of Gondwana: Geological Society of London, Special Publications, v. 550, doi:10.1144/SP550-2024-36.

Gómez-Pérez, I., Al Rawahi, H., and Bergmann, K.D., 2024a, An integrated correlation from platform to basin: implications for understanding the Ediacaran succession of Oman: American Association of Petroleum Geologists, Bulletin, v. 108, p. 1727–1766, doi:10.1306/03222423009.

Gómez-Pérez, I., Morton, A., Rawahi, H.A., and Frei, D., 2024b, Oman as a fragment of Ediacaran eastern Gondwana: Geology, v. 52, p. 473–478, doi:10.1130/G51989.1.

Gonzalez, L.A., and Lohmann, K.C, 1988, Controls on mineralogy and composition of spelean carbonates: Carlsbad Caverns, New Mexico, *in* James, N.P., and Choquette, P.W., eds., Paleokarst: New York, Springer-Verlag, p. 81–101, doi:10.1007/978-1-4612-3748-8_4.

Gorin, G.E., Racz, L.G., and Walter, M.R., 1982, Late Precambrian–Cambrian sediments of Huqf Group, Sultanate of Oman: American Association of Petroleum Geologists, Bulletin, v. 66, p. 2609–2627, doi:10.1306/03B5AC82-16D1-11D7-8645000102C1865D.

Grélaud, C., Razin, P., Homewood, P.W., and Schwab, A.M., 2006, Development of incisions on a periodically emergent carbonate platform (Natih Formation, Late Cretaceous, Oman): Journal of Sedimentary Research, v. 76, p. 647–669, doi:10.2110/jsr.2006.058.

Grotzinger, J.P., 1986, Cyclicity and paleoenvironmental dynamics, Rocknest platform, northwest Canada: Geological Society of America, Bulletin, v. 97, p. 1208–1231, doi:10.1130/0016-7606(1986)97<1208:CAPDRP>2.0.CO;2.

Grotzinger, J.P., and Al-Rawahi, Z., 2014, Depositional facies and platform architecture of microbialite-dominated carbonate reservoirs, Ediacaran–Cambrian Ara Group, Sultanate of Oman: American Association of Petroleum Geologists, Bulletin, v. 98, p. 1453–1494, doi:10.1306/02271412063.

Grotzinger, J.P., and James, N.P., 2000, Precambrian carbonates: evolution of understanding, *in* Grotzinger, J.P., and James, N.P., eds., Carbonate Sedimentation and Diagenesis in the Evolving Precambrian World: SEPM, Special Publication 67, p. 3–20, doi:10.2110/pec.00.67.

Grover, G., Jr., and Read, J., 1983, Paleoaquifer and deep burial related cements defined by regional cathodoluminescent patterns, Middle Ordovician carbonates, Virginia: American Association of Petroleum Geologists, Bulletin, v. 67, p. 1275–1303.

Gulley, J., Martin, J., and Moore, P., 2014, Vadose CO_2 gas drives dissolution at water tables in eogenetic karst aquifers more than mixing dissolution: Earth Surface Processes and Landforms, v. 39, p. 1833–1846, doi:10.1002/esp.3571.

Halverson, G.P., Hoffman, P.F., Schrag, D.P., Maloof, A.C., and Rice, A.H.N., 2005, Toward a Neoproterozoic composite carbon-isotope record: Geological Society of America, Bulletin, v. 117, p. 1181–1207, doi:10.1130/B25630.1.

Harrison, R.S., and Steinen, R.P., 1978, Subaerial crusts, caliche profiles, and breccia horizons: comparison of some Holocene and Mississippian exposure surfaces, Barbados and Kentucky: Geological Society of America, Bulletin, v. 89, p. 385–396, doi:10.1130/0016-7606(1978)89<385:SCCPAB>2.0.CO;2.

He, J., Qing, H., and Xu, B., 2019, The unconformity-related palaeokarst in the uppermost Ediacaran carbonate rocks in the northwestern Tarim Block, NW China: implication for sedimentary evolution during the Ediacaran–Cambrian transition: International Geology Review, v. 61, p. 839–852, doi:10.1080/00206814.2018.1474498.

Holland, H.D., and Zbinden, E.A., 1988, Paleosols and the evolution of the atmosphere: Part I, *in* Lerman, A., and Meybeck, M., eds., Physical and Chemical Weathering in Geochemical Cycles: Dordrecht, Springer, p. 61–82, doi:10.1007/978-94-009-3071-1_4.

James, N.P., and Choquette, P.W., (eds.), 1988, Paleokarst: New York, Springer-Verlag, 416 p.

James, N.P., Narbonne, G.M., and Kyser, T.K., 2001, Late Neoproterozoic cap carbonates: Mackenzie Mountains, northwestern Canada: precipitation and global glacial meltdown: Canadian Journal of Earth Sciences, v. 38, p. 1229–1262, doi:10.1139/e01-046.

Johnson, P.R., and Woldehaimanot, B., 2003, Development of the Arabian–Nubian Shield: perspectives on accretion and deformation in the northern East African Orogen and the assembly of Gondwana: Geological Society of London, Special Publications, v. 206, p. 289–325, doi:10.1144/GSL.SP.2003.206.01.15.

Jolliffe, A.W., 1955, Geology and iron ores of Steep Rock Lake (Ontario): Economic Geology, v. 50, p. 373–398, doi:10.2113/gsecongeo.50.4.373.

Kelley, B.M., Lehrmann, D.J., Yu, M., Jost, A.B., Meyer, K.M., Lau, K.V., Altiner, D., Li, X., Minzoni, M., Schaal, E.K., and Payne, J.L., 2020, Controls on carbonate platform architecture and reef recovery across the Palaeozoic to Mesozoic transition: a high-resolution analysis of the Great Bank of Guizhou: Sedimentology, v. 67, p. 3119–3151, doi:10.1111/sed.12741.

Kelley, B.M., Lehrmann, D.J., Yu, M., Lau, K.V., Altiner, D., Minzoni, M., Enos, P., Li, X., and Payne, J.L., 2024, Metazoan–algal benthic ecosystems enhance automicritic slope boundstone: the Triassic Great Bank of Guizhou carbonate platform, Xiliang margin, China: American Association of Petroleum Geologists, Bulletin, v. 108, p. 1851–1884, doi:10.1306/06112422064.

Kendall, C.G.St.C., 1969, An environmental re-interpretation of the Permian evaporite/carbonate shelf sediments of the Guadalupe Mountains: Geological Society of America, Bulletin, v. 80, p. 2503–2526, doi:10.1130/0016-7606(1969)80[2503:AEROTP]2.0.CO;2.

Kennard, J.M., and James, N.P., 1986, Thrombolites and stromatolites: two distinct types of microbial structures: Palaios, v. 1, p. 492–503, doi:10.2307/3514631.

Kenny, R., and Knauth, L.P., 1992, Continental paleoclimates from δD and $\delta^{18}O$ of secondary silica in paleokarst chert lags: Geology, v. 20, p. 219–222, doi:10.1130/0091-7613(1992)020<0219:CPFDAO>2.3.CO;2.

Kenter, J.A.M., Harris, P.M., and Della Porta, G., 2005, Steep microbial boundstone-dominated platform margins—examples and implications: Sedimentary Geology, v. 178, p. 5–30, doi:10.1016/j.sedgeo.2004.12.033.

Kerans, C., 1988, Karst-controlled reservoir heterogeneity in Ellenburger Group carbonates of West Texas: American Association of Petroleum Geologists, Bulletin, v. 72, p. 1160–1183, doi:10.1306/703C996F-1707-11D7-8645000102C1865D.

Kerans, C., 1993, Description and interpretation of karst-related breccia fabrics, Ellenburger Group, West Texas, *in* Fritz, R.D., Wilson, J.L., and Yurewicz, D.A., eds., Paleokarst Related Hydrocarbon Reservoirs: SEPM, Core Workshop 18, p. 181–200, http://archives.datapages.com/data/sepm_sp/CW18/Description_and_Interpretation.htm.

Kerans, C., and Donaldson, J.A., 1988, Proterozoic paleokarst profile, Dismal Lakes Group, NWT, Canada, *in* James, N.P., and Choquette, P.W., eds., Paleokarst: New York, Springer-Verlag, p. 167–182.

Kerans, C., and Tinker, S.W., 1997, Sequence stratigraphy and characterization of carbonate reservoirs: http://scnotes.sepmonline.org/content/sepscseq/1.toc.

Kerans, C., and Tinker, S.W., 1999, Extrinsic stratigraphic controls on development of the Capitan Reef Complex, *in* Saller, A.H., Harris, P.M., Kirkland, B.L., and Mazzullo, S.J., eds., Geologic Framework of the Capitan Reef: SEPM, Special Publication 65, p. 15–36.

Krissansen-Totton, J., Arney, G.N., and Catling, D.C., 2018, Constraining the climate and ocean pH of the early Earth with a geological carbon cycle model: National Academy of Sciences [U.S.A.], Proceedings, v. 115, p. 4105–4110, doi:10.1073/pnas.1721296115.

Loosveld, R.J.H., Bell, A., and Terken, J.J.M., 1996, The tectonic evolution of interior Oman: GeoArabia, v. 1, p. 28–51, doi:10.2113/geoarabia010128.

Loucks, R.G., 1999, Paleocave carbonate reservoirs: origins, burial-depth modifications, spatial complexity, and reservoir implications1: American Association of Petroleum Geologists, Bulletin, v. 83, p. 1795–1834, doi:10.1306/E4FD426F-1732-11D7-8645000102C1865D.

Lucia, F.J., 1995, Lower Paleozoic cavern development, collapse, and dolomitization, Franklin Mountains, El Paso, Texas, *in* Budd, D.A., Saller, A.H., and Harris, P.M., eds., Unconformities and Porosity in Carbonate Strata: American Association of Petroleum Geologists, Memoir 63, p. 279–300, doi:10.1306/M63592.

Lucia, F.J., 1999, Diagenetic overprinting and rock-fabric distribution: the massive dissolution, collapse, and fracturing environment, *in* Lucia, F.J., ed., Carbonate Reservoir Characterization: Berlin, Springer, p. 157–176, doi:10.1007/978-3-662-03985-4_7.

Machado, A.D.B., 1987, On the origin and age of the Steep Rock buckshot, Ontario, Canada: Chemical Geology, v. 60, p. 337–349, doi:10.1016/0009-2541(87)90141-0.

Mathieu, J., Turner, E.C., and Rainbird, R.H., 2017, Origin and hydrology of a large, intact Early Cambrian paleocave system and its role in overlying fluidisation structures, Arctic Canada: Sedimentary Geology, v. 351, p. 66–79, doi:10.1016/j.sedgeo.2017.02.006.

Matter, A., and Burns, S.J., 1993, Carbon isotopic record of the latest Proterozoic from Oman: Eclogae Geologicae Helvetiae, v. 86, p. 595–607, doi:10.5169/SEALS-167254.

Mattes, B.W., and Conway Morris, S., 1990, Carbonate/evaporite deposition in the Late Precambrian–Early Cambrian Ara Formation of Southern Oman, *in* Robertson, A.H., Searle, M.P., and Ries, A.C., eds., The Geology and Tectonics of the Oman Region: Geological Society of London, Special Publications, v. 49, p. 617–636, doi:10.1144/GSL.SP.1992.049.01.37.

Mazzullo, S.J., and Birdwell, B.A., 1989, Syngenetic formation of grainstones and pisolites from fenestral carbonates in peritidal settings: Journal of Sedimentary Petrology, v. 59, p. 605–611, doi:10.1306/212f9002-2b24-11d7-8648000102c1865d.

Moore, K., Crémière, A., Present, T.M., Barnett, A.J., Bergmann, K.D., Amthor, J.E., and Grotzinger, J.P., 2024, Primary microfossiliferous chert in the Aptian Barra Velha Formation: Sedimentology, v. 71, p. 1815–1842, doi:10.1111/sed.13193.

Mustard, P.S., and Donaldson, J.A., 1990, Paleokarst breccias, calcretes, silcretes and fault talus breccias at the base of upper Proterozoic Windermere strata, northern Canadian Cordillera: Journal of Sedimentary Research, v. 60, p. 525–539, doi:10.1306/212F91D8-2B24-11D7-8648000102C1865D.

Mutti, M.E., and Simo, J.A., 1993, Stratigraphic patterns and cycle-related diagenesis of upper Yates Formation, Permian, Guadalupe Mountains, *in* Loucks, R.G., and Sarg, J.F., eds., Carbonate Sequence Stratigraphy: Recent Developments and Applications: American Association of Petroleum Geologists, Memoir 57, p. 515–534.

Mylroie, J.E., and Carew, J.L., 1988, Solution conduits as indicators of late Quaternary sea level position: Quaternary Science Reviews, v. 7, p. 55–64, doi:10.1016/0277-3791(88)90093-5.

Mylroie, J.E., and Carew, J.L., 1990, The flank margin model for dissolution cave development in carbonate platforms: Earth Surface Processes and Landforms, v. 15, p. 413–424, doi:10.1002/esp.3290150505.

Mylroie, J.E., and Carew, J.L., 1995, Karst development on carbonate islands, *in* Budd, D.A., Saller, A.H., and Harris, P.M., eds., Unconformities and Porosity in Carbonate Strata: American Association of Petroleum Geologists, Memoir 63, p. 55–76, http://archives.datapages.com/data/specpubs/memoir63/chapt12/0239.htm.

Mylroie, J.R., and Mylroie, J.E., 2007, Development of the Carbonate Island Karst Model: Journal of Cave and Karst Studies, v. 69, p. 59–75.

Nicholas, C.J., and Gold, S.E.P., 2012, Ediacaran–Cambrian Sirab Formation of the Al Huqf region, Sultanate of Oman: GeoArabia, v. 17, p. 49–98.

Nolting, A., Kerans, C., Fernandez-Ibanez, F., Fullmer, S., Moore, P.J., Breithaupt, C.I., LeBlanc, S., Dafov, M., Bunge, E., and Gulley, J., 2024, Three-dimensional stratigraphic architecture, secondary pore system development and the Middle Pleistocene transition, Sandy Point area, San Salvador Island, Bahamas: Sedimentology, v. 71, p. 207–240, doi:10.1111/sed.13134.

Osburn, M., Grotzinger, J., and Bergmann, K., 2014, Facies, stratigraphy, and evolution of a middle Ediacaran carbonate ramp: Khufai Formation, Sultanate of Oman: American Association of Petroleum Geologists, Bulletin, v. 98, p. 1631–1667.

Pelechaty, S.M., James, N.P., Kerans, C., and Grotzinger, J.P., 1991, A middle Proterozoic palaeokarst unconformity and associated sedimentary rocks, Elu Basin, northwest Canada: Sedimentology, v. 38, p. 775–797, doi:10.1111/j.1365-3091.1991.tb01872.x.

Petterson, R., Prave, A.R., Wernicke, B.P., and Fallick, A.E., 2011, The Neoproterozoic Noonday Formation, Death Valley region, California: Geological Society of America, Bulletin, v. 123, p. 1317–1336, doi:10.1130/B30281.1.

Playton, T.E., and Kerans, C., 2018, Architecture and genesis of prograding deep boundstone margins and debris-dominated carbonate slopes: examples from the Permian Capitan Formation, Southern Guadalupe Mountains, West Texas: Sedimentary Geology, v. 370, p. 15–41, doi:10.1016/j.sedgeo.2017.12.021.

Plummer, L.N., 1975, Mixing of sea water with calcium carbonate ground water, *in* Whitten, E.H.T., ed., Quantitative Studies in the Geological Sciences: Geological Society of America, Memoir 142, p. 219–236, doi:10.1130/MEM142-p219.

Pope, M.C., Grotzinger, J.P., and Schreiber, B.C., 2000, Evaporitic subtidal stromatolites produced by in situ precipitation: textures, facies associations, and temporal significance: Journal of Sedimentary Research, v. 70, p. 1139–1151, doi:10.1306/062099701139.

Praekelt, H.E., Germs, G.J.B., and Kennedy, J.H., 2008, A distinct unconformity in the Cango Caves Group of the Neoproterozoic to early Paleozoic Saldania Belt in South Africa: its regional significance: South African Journal of Geology, v. 111, p. 357–368, doi:10.2113/gssajg.111.4.357.

Pratt, B.R., 1984, Epiphyton and Renalcis: diagenetic microfossils from calcification of coccoid blue-green algae: Journal of Sedimentary Petrology, v. 54, p. 948–971, doi:10.1306/212F853F-2B24-11D7-8648000102C1865D.

Present, T.M., Gomes, M.L., Trower, E.J., Stein, N.T., Lingappa, U.F., Naviaux, J., Thorpe, M.T., Cantine, M.D., Fischer, W.W., Knoll, A.H., and Grotzinger, J.P., 2021, Non-lithifying microbial ecosystem dissolves peritidal lime sand: Nature Communications, v. 12, p. 1–8, doi:10.1038/s41467-021-23006-1.

Purkis, S.J., Rowlands, G.P., Riegl, B.M., and Renaud, P.G., 2010, The paradox of tropical karst morphology in the coral reefs of the arid Middle East: Geology, v. 38, p. 227–230, doi:10.1130/G30710.1.

Rajaibi, I.M.A., Hollis, C., and Macquaker, J.H., 2015, Origin and variability of a terminal Proterozoic primary silica precipitate, Athel Silicilyte, South Oman Salt Basin, Sultanate of Oman: Sedimentology, v. 62, p. 793–825, doi:10.1111/sed.12173.

Rankey, E.C., and Bachtel, S.L., 1998, Subaerial exposure surfaces in carbonate strata: their recognition and significance, *in* Cox, D.M., ed., Upper Pennsylvanian and Wolfcampian Mixed Carbonate–Siliclastic Systems, Sacramento Mountains, New Mexico: outcrop models for subsurface plays and reservoir development: Midland, Texas, West Texas Geological Society, Annual Field Trip Guidebook 98–104, p. 115–136.

Reid, R.P., Visscher, P.T., Decho, A.W., Stolz, J.F., Bebout, B.M., Dupraz, C., Macintyre, I.G., Paerl, H.W., Pinckney, J.L., and Prufert-Bebout, L., 2000, The role of microbes in accretion, lamination and early lithification of modern marine stromatolites: Nature, v. 406, p. 989–992.

Riding, R., 1991, Calcified cyanobacteria, *in* Riding, R., ed., Calcareous Algae and Stromatolites: Berlin, Springer, p. 55–87, doi:10.1007/978-3-642-52335-9.
Rivers, J.M., 2023, Warm acidified seawater: a dolomite solution: Journal of Sedimentary Research, v. 93, p. 187–201, doi:10.2110/jsr.2022.087.
Rivers, J.M., and Dalrymple, R.W., 2025, The reconstruction of coastal carbonate sequence stratigraphy: a modern-systems approach: Geology, v. 53, p. 232–237, doi:10.1130/G52776.1.
Rivers, J.M., and Kaczmarek, S.E., 2020, Dologrus: the impact of meteoric-water-controlled diagenesis following early-marine dolomitization: Sedimentology, v. 67, p. 3317–3332, doi:10.1111/sed.12742.
Rivers, J.M., Engel, M., Dalrymple, R., Yousif, R., Strohmenger, C.J., and Al-Shaikh, I., 2020, Are carbonate barrier islands mobile? Insights from a mid to late-Holocene system, Al Ruwais, northern Qatar: Sedimentology, v. 67, p. 534–558, doi:10.1111/sed.12653.
Rivers, J.M., Yousif, R., Kaczmarek, S.E., and Al-Shaikh, I., 2021, Cenozoic coastal carbonate deposits of Qatar: evidence for dolomite preservation bias in highly-arid systems: Sedimentology, v. 68, p. 771–787, doi:10.1111/sed.12805.
Rush, J.W., 2022, Comparative Sedimentology of Modern and Ancient Oolitic Sand Shoals and Tidal Deltas [Ph.D. Thesis]: University of Kansas, Lawrence, 337 p.
Rush, J., and Kerans, C., 2010, Stratigraphic response across a structurally dynamic shelf: the latest Guadalupian composite sequence at Walnut Canyon, New Mexico, U.S.A.: Journal of Sedimentary Research, v. 80, p. 808–828, doi:10.2110/jsr.2010.073.
Rush, J.W., and Rankey, E.C., 2017, Geostatistical facies modeling trends for oolitic tidal sand shoals: American Association of Petroleum Geologists, Bulletin, v. 101, p. 1341–1379, doi:10.1306/09221616032.
Sami, T.T., and James, N.P., 1994, Peritidal carbonate platform growth and cyclicity in an early Proterozoic foreland basin, upper Pethei Group, Northwest Canada: Journal of Sedimentary Research, v. 64, p. 111–131, doi:10.1306/D4267F6E-2B26-11D7-8648000102C1865D.
Santos, L. da R., Cury, L.F., Rosenblume, J., Mendes, M.T., Fedalto, G., Lopes, A.P., Leandro, R., Siga, O., Jr., and Basei, M., 2022, Tracing the continental margins of the Southern Ribeira belt, Brazil: provenance and connections of post-Rodinia fragments: Precambrian Research, v. 378, doi:10.1016/j.precamres.2022.106756.
Santos, L. da R., Fedalto, G., Bahniuk, A.M., Casapula, I., Oliveira, F., and Cury, L.F., 2023, The formation and evolution of Al-rich protoliths in the southern Ribeira belt, Brazil: insights from remnants of a Precambrian paleoweathering surface: Earth Surface Processes and Landforms, p. 1–27, doi:10.1002/esp.5671.
Schoenherr, J., Reuning, L., Kukla, P.A., Littke, R., Urai, J.L., Siemann, M., and Rawahi, Z., 2009, Halite cementation and carbonate diagenesis of intra-salt reservoirs from the Late Neoproterozoic to Early Cambrian Ara Group (South Oman Salt Basin): Sedimentology, v. 56, p. 567–589, doi:10.1111/j.1365-3091.2008.00986.x.
Schröder, S., and Grotzinger, J.P., 2007, Evidence for anoxia at the Ediacaran–Cambrian boundary: the record of redox-sensitive trace elements and rare earth elements in Oman: Geological Society of London, Journal, v. 164, p. 175–187, doi:10.1144/0016-76492005-022.
Schröder, S., Schreiber, B.C., Amthor, J.E., and Matter, A., 2003, A depositional model for the terminal Neoproterozoic–Early Cambrian Ara Group evaporites in south Oman: Sedimentology, v. 50, p. 879–898, doi:10.1046/j.1365-3091.2003.00587.x.
Schröder, S., Grotzinger, J.P., Amthor, J.E., and Matter, A., 2005, Carbonate deposition and hydrocarbon reservoir development at the Precambrian–Cambrian boundary: the Ara Group in South Oman: Sedimentary Geology, v. 180, p. 1–28, doi:10.1016/j.sedgeo.2005.07.002.
Shride, A.F., 1967, Younger Precambrian Geology in Southern Arizona: U.S. Geological Survey, Professional Paper 566, 94 p.
Skotnicki, S.J., and Knauth, L.P., 2007, The middle Proterozoic Mescal Paleokarst, central Arizona, U.S.A.: karst development, silicification, and cave deposits: Journal of Sedimentary Research, v. 77, p. 1046–1062, doi:10.2110/jsr.2007.094.
Smith, B.P., Cantine, M.D., Bergmann, K.D., Ramos, E.J., Martindale, R.C., and Kerans, C., 2021, Arid coastal carbonates and the Phanerozoic record of carbonate chemistry: American Geophysical Union, Advances, v. 2, doi:10.1029/2021AV000386.
Southard, J.B., Lambie, J.M., Federico, D.C., Pile, H.T., and Weidman, C.R., 1990, Experiments on bed configurations in fine sands under bidirectional purely oscillatory flow, and the origin of hummocky cross-stratification: Journal of Sedimentary Petrology, v. 60, p. 1–17, doi:10.1306/212f90f7-2b24-11d7-8648000102c1865d.
Stoessell, R.K., Moore, Y.H., and Coke, J.G., 1993, The occurrence and effect of sulfate reduction and sulfide oxidation on coastal limestone dissolution in Yucatan cenotes: Groundwater, v. 31, p. 566–575.
Strauss, J.V., and Tosca, N.J., 2020, Mineralogical constraints on Neoproterozoic pCO_2 and marine carbonate chemistry: Geology, v. 48, p. 599–603, doi:10.1130/G47506.1.
Stuart-Smith, P.G., Romine, K., Teasdale, J., and Schreurs, J.M., 2007, Basement control on structure and evolution of the salt basins of Oman [Abstract]: GEO 2006 Middle East Conference and Exhibition, GeoArabia, v. 12, p. 193.
Tang, P., Chen, D., Wang, Y., Ding, Y., El-Shafeiy, M., and Yang, B., 2021, Diagenesis of microbialite-dominated carbonates in the Upper Ediacaran Qigebrak Formation, NW Tarim Basin, China: implications for reservoir development: Marine and Petroleum Geology, v. 136, doi:10.1016/j.marpetgeo.2021.105476.
Teitz, M.W., 1985, Late Proterozoic Yellowhead and Astoria Carbonate Platforms, southwest of Jasper, Alberta [M.S. Thesis]: McGill University, Montreal.
Teitz, M.W., and Mountjoy, E.W., 1989, The Late Proterozoic Yellowhead Carbonate Platform west of Jasper, Alberta, *in* Geldsetzer, H.H.J., James, N.P., and Tebbutt, G.E., eds., Reefs: Canada and Adjacent Area: Canadian Society of Petroleum Geologists, Memoir 13, p. 129–134.
Tinker, S.W., Ehrets, J.R., and Brondos, M.D., 1995, Multiple karst events related to stratigraphic cyclicity: San Andres Formation, Yates Field, West Texas, *in* Budd, D.A., Saller, A.H., and Harris, P.M., eds., Unconformities and Porosity in Carbonate Strata: American Association of Petroleum Geologists, Memoir 63, p. 213–237, https://archives.datapages.com/data/specpubs/memoir63/chapt11/0213.htm.
Turner, E.C., James, N.P., and Narbonne, G.M., 2000, Taphonomic control on microstructure in early Neoproterozoic reefal stromatolites and thrombolites: Palaios, v. 15, p. 87–111, doi:10.2307/3515496.
Turner, E.C., and Long, D.G.F., 2012, Formal definition of the Neoproterozoic Mackenzie Mountains Supergroup (Northwest Territories), and formal stratigraphic nomenclature for its carbonate and evaporite formations: Geological Survey of Canada, Open File 7112, 57 p., doi:10.4095/292167.
Urlwin, B., 1997, Neoproterozoic carbonates of the Jasper region: sedimentology, stratigraphy and stromatolite morphology [M.S. Thesis]: University of Calgary, 240 p., doi:10.11575/PRISM/21884.
Vahrenkamp, V.C., and Rossinsky, V., Jr., 1987, Preserved stable isotopic signature of subaerial diagenesis in the Mescal Limestone, central Arizona: implications for the timing of a terrestrial plant cover: Discussion and reply: Discussion: Geological Society of America, Bulletin, v. 99, p. 595–596, doi:10.1130/0016-7606(1987)99<595:PSISOS>2.0.CO;2.
Vahrenkamp, V.C., David, F., Duijndam, P., Newall, M., and Crevello, P., 2004, Growth architecture, faulting, and karstification of a middle Miocene carbonate platform, Luconia Province, Offshore Sarawak, Malaysia, *in* Eberli, G.P., Masaferro, J.L., and Sarg, J.F., eds., Seismic Imaging of Carbonate Reservoirs and Systems: American Association of Petroleum Geologists, Memoir 81, p. 329–350.
Wallace, M.W., Hood, A.V.S., Woon, E.M.S., Giddings, J.A., and Fromhold, T.A., 2015, The Cryogenian Balcanoona reef complexes of the Northern Flinders Ranges: implications for Neoproterozoic ocean chemistry: Palaeogeography, Palaeoclimatology, Palaeoecology, v. 417, p. 320–336, doi:10.1016/j.palaeo.2014.09.028.
Walter, L.M., and Burton, E.A., 1990, Dissolution of Recent platform carbonate sediments in marine pore fluids: American Journal of Science, v. 290, p. 601–643, doi:10.2475/ajs.290.6.601.
Walter, L.M., Bischof, S.A., Patterson, W.P., Lyons, T.W., O'Nions, R.K., Gruszczynski, M., Sellwood, B.W., and Coleman, M.L., 1993, Dissolution and recrystallization in modern shelf carbonates: evidence from pore water and solid phase chemistry [and Discussion]: Royal Society of London, Philosophical Transactions, Series A, Physical and Engineering Sciences, v. 344, p. 27–36, doi:10.1098/rsta.1993.0072.
Woodcock, N.H., Omma, J.E., and Dickson, J.A.D., 2006, Chaotic breccia along the Dent Fault, NW England: implosion or collapse of a fault void?: Geological Society of London, Journal, v. 163, p. 431–446, doi:10.1144/0016-764905-067.
Wright, V.P., 1982, Calcrete palaeosols from the lower carboniferous Llanelly Formation, South Wales: Sedimentary Geology, v. 33, p. 1–33, doi:10.1016/0037-0738(82)90025-2.
Wright, V.P., 1990, A micromorphological classification of fossil and recent calcic and petrocalcic microstructures, *in* Douglas, L.A., ed., Developments in Soil Science: Elsevier, p. 401–407, doi:10.1016/S0166-2481(08)70354-4.
Wright, V.P., 1994, Paleosols in shallow marine carbonate sequences: Earth-Science Reviews, v. 35, p. 367–395, doi:10.1016/0012-8252(94)90002-7.

Received 31 July 2025; accepted 24 March 2026.